

Blast-induced liquefaction in silty sands for full-scale testing of ground improvement methods: Insights from a multidisciplinary study

Original

Blast-induced liquefaction in silty sands for full-scale testing of ground improvement methods: Insights from a multidisciplinary study / Amoroso, S.; Rollins, K. M.; Andersen, P.; Gottardi, G.; Tonni, L.; Garcia Martinez, M. F.; Wissmann, K.; Minarelli, L.; Comina, C.; Fontana, D.; De Martini, P. M.; Monaco, P.; Pesci, A.; Sapia, V.; Vassallo, M.; Anzidei, M.; Carpena, A.; Cinti, F.; Civico, R.; Coco, I.; Conforti, D.; Doumaz, F.; Giannattasio, F.; Di Giulio, G.; Foti, S.; Loddo, F.; Lugli, S.; Manuel, M. R.; Marchetti, D.; Mariotti, M.; Materni, V.; Metcalfe, B.; Milana, G.; Pantosti, D.; Pesce, A.; Salocchi, A. C.; Smedile, A.; Stefani, M.; Tarabusi, G.; Teza, G.. - In: ENGINEERING GEOLOGY. - ISSN 0013-7952. - 265 (2020), p. 105437. [10.1016/j.enggeo.2019.105437]
This version is available at: 11583/2788192 since: 2020-02-06T12:37:27Z

Publisher:

Elsevier B.V.

Published

DOI:10.1016/j.enggeo.2019.105437

Terms of use:

This article is made available under terms and conditions as specified in the corresponding bibliographic description in the repository

Publisher copyright

Elsevier postprint/Author's Accepted Manuscript

© 2020. This manuscript version is made available under the CC-BY-NC-ND 4.0 license
<http://creativecommons.org/licenses/by-nc-nd/4.0/>. The final authenticated version is available online at:
<http://dx.doi.org/10.1016/j.enggeo.2019.105437>

(Article begins on next page)

1 Blast-induced liquefaction in silty sands for full-scale testing of ground improvement
2 methods: insights from a multidisciplinary study
3

4 Sara Amoroso^{a, b}, Kyle M. Rollins^c, Paul Andersen^c, Guido Gottardi^d, Laura Tonni^d, Maria F.
5 García Martínez^d, Kord Wissmann^e, Luca Minarelli^b, Cesare Comina^f, Daniela Fontana^g, Paolo
6 Marco De Martini^h, Paola Monacoⁱ, Arianna Pesci^j, Vincenzo Sapia^h, Maurizio Vassallo^b, Marco
7 Anzidei^h, Andrea Carpena^k, Francesca Cinti^h, Riccardo Civico^h, Iginio Coco^h, Dario Conforti^l, Fawzi
8 Doumaz^h, Fabio Giannattasio^h, Giuseppe Di Giulio^b, Sebastiano Foti^m, Fabiana Loddo^j, Stefano
9 Lugli^g, Maria R. Manuelⁿ, Diego Marchetti^o, Mauro Mariotti^p, Valerio Materni^h, Brian Metcalfe^e,
10 Giuliano Milana^h, Daniela Pantosti^h, Antonio Pesce^f, Aura C. Salocchi^g, Alessandra Smedile^h,
11 Marco Stefani^q, Gabriele Tarabusi^j, Giordano Teza^r

12
13 ^a*Department of Engineering and Geology, University of Chieti-Pescara, Viale Pindaro 42, 65129 Pescara, Italy*

14 ^b*Istituto Nazionale di Geofisica e Vulcanologia, viale Crispi 43, 67100 L'Aquila, Italy*

15 ^c*Department of Civil and Environmental Engineering, Brigham Young University, 430 Engineering Building, Provo,*
16 *Utah 84602, USA*

17 ^d*Department of Civil, Chemical, Environmental, and Materials Engineering, University of Bologna, Viale del*
18 *Risorgimento 2, 40136 Bologna, Italy*

19 ^e*Geopier Foundation Company, 130 Harbour Place Drive, Davidson, North Carolina 28036*

20 ^f*Department of Earth Sciences, University of Turin, via Valperga Caluso 35, 10125 Torino, Italy*

21 ^g*Department of Chemical and Geological Sciences, University of Modena and Reggio Emilia, via Campi 103, 41125*
22 *Modena, Italy*

23 ^h*Istituto Nazionale di Geofisica e Vulcanologia, via di Vigna Murata 605, 00143 Rome, Italy*

24 ⁱ*Department of Civil, Construction-Architectural and Environmental Engineering, University of L'Aquila, Piazzale*
25 *Ernesto Pontieri, Monteluco di Roio, 67100 L'Aquila, Italy*

26 ^j*Istituto Nazionale di Geofisica e Vulcanologia, via Donato Creti 12, 40128 Bologna, Italy*

27 ^k*Georeflex srl, via Carlo Fioruzzi 15, 29121 Piacenza, Italy*

28 ^l*Teledyne Optech Incorporated, 300 Interchange Way, Vaughan, Ontario, L4K 5Z8 Canada*

^mDepartment of Structural, Building and Geotechnical Engineering, Politecnico di Torino, corso Duca degli Abruzzi
24, 10129 Turin, Italy

ⁿGEO Geotecnica e Geognostica srl, Via Faucio 16, 03033 Arpino, Italy,

^oStudio Prof. Marchetti srl, via Bracciano 38, 00189 Rome, Italy

^pSara Electronic Instruments srl, Via A. Mercuri 4, 06129 Perugia, Italy

^qDepartment of Architecture, University of Ferrara, Via della Ghiara 36, 44121 Ferrara, Italy

^rDepartment of Geosciences, University of Padua, via Gradenigo 6, 35131 Padua, Italy

36

HIGHLIGHTS

Blast tests produced liquefaction and sand boils at a silty sand site in northern Italy

Blast tests produced volumetric strain similar to that expected in an earthquake

Aggregate piers as a liquefaction hazard mitigation strategy improved soil performance

Geophysical and geotechnical site investigations were carried out before and after blasting

Field responses of treated and non-treated soils during blasting were compared

43

ABSTRACT

In the engineering geology field increased attention has been posed in recent years to potential liquefaction mitigation interventions in susceptible sand formations. In silty sands this is a major challenge because, as the fines content increases, vibratory methods for densification become progressively less effective. An alternative mitigation technique can be the installation of Rammed Aggregate Pier® (RAP) columns that can increase the resistance of the soil, accounting for its lateral stress increase and for the stiffness increase from soil and RAP composite response. To investigate the influence of these factors on liquefaction resistance, full-scale blast tests were performed at a silty sand site in Bondeno (Ferrara, Italy) where liquefaction was observed after the 2012 Emilia-Romagna earthquake. A multidisciplinary team of forty researchers carried out devoted experimental activities aimed at better understanding the liquefaction process at the field scale and the effectiveness of the treatment using inter-related methods. Both natural and improved

56 areas were investigated by in-situ tests and later subjected to controlled blasting. The blast tests
57 were monitored with geotechnical and geophysical instrumentation, topographical surveying and
58 geological analyses on the sand boils. Results showed the RAP effectiveness due to the
59 improvement of soil properties within the liquefiable layer and a consequent reduction of the blast-
60 induced liquefaction settlements, likely due to soil densification and increased lateral stress. The
61 applied multidisciplinary approach adopted for the study allowed better understanding of the
62 mechanism involved in the liquefaction mitigation intervention and provided a better overall
63 evaluation of mitigation effectiveness.

64

65 *Keywords:* liquefaction, blast test, rammed aggregate piers, ground improvement, silty sands,
66 Emilia-Romagna earthquake

67

68 **1. Introduction**

69 The identification of an effective soil improvement technique for the mitigation of liquefaction
70 hazard in silty sand deposits is undoubtedly a major challenge for engineers, geologists, building
71 owners, developers, and specialty contractors. Indeed, as the fines content increases, the normally
72 adopted vibratory methods for densification become progressively less effective and therefore more
73 expensive approaches, such as soil mixing or deep foundations, are often required. Most of these
74 alternative techniques are based on the installation of stiffer elements within the soil aimed at
75 increasing both strength and soil density: typical examples are the Rammed Aggregate Piers®
76 (RAP), Stone Columns (SC), Low Mobility Grout (LMG) or Timber Displacement Pile (TDP). In
77 recent years, the Resonant Compaction Method (RCM) has also been investigated as a ground
78 improvement solution in liquefaction-prone silts-silty sands (e.g. Li et al., 2018).

79 Over the last decades, a large amount of research has been carried out on liquefaction mitigation in
80 clean sands, especially with reference to ground improvement techniques by densification. In recent
81 years research interest has been also extended to liquefaction-prone deposits of silts and silty sands.

82 It is worth mentioning here the valuable outcomes from the extensive investigations carried out in
83 Christchurch (New Zealand), following the widespread liquefaction and lateral spreading evidences
84 due to the 2010-2011 Canterbury earthquake sequence (Giona Bucci et al., 2018). Wissmann et al.
85 (2015), Vautherin et al. (2017), and Amoroso et al. (2018) examined the performance of RAP
86 installation, showing that densification can be obtained and reliably quantified by means of
87 piezocone (CPTU) and flat dilatometer (DMT) measurements in granular soil deposits having a soil
88 behaviour type index $I_c < 1.8$ or a material index $I_D > 1.8$, also at depths exceeding the design
89 treatment depth. Wotherspoon et al. (2015) and Hwang et al. (2017) assessed the effectiveness of
90 soil stiffening caused by the installation of SC, RAP and LMG using cross-hole tests. RAP
91 appeared to produce stiffer discrete inclusions than SC, while LMG column installation actually
92 compromised the liquefaction resistance. Finally, Alexander et al. (2017) examined the performance
93 of a SC foundation system subjected to the Canterbury earthquake, showing that SC can cause
94 contamination of gravel with silty fines and prevent drainage during shaking, thus resulting in loss
95 of performance.

96 After the 1991 Loma Prieta earthquake, mitigation strategies against liquefaction in silty sands were
97 also analyzed by Mitchell and Wentz (1991), who compared the performance of sites reinforced by
98 SC with that of adjacent untreated areas. Minor or negligible damage was observed in the improved
99 soils, whereas cracks and/or settlements, primarily due to liquefaction, occurred in untreated soil
100 deposits. However, as the non-plastic fines content increased, the SC technique appeared to be more
101 successful in combination with pre-installed wick drains (Adalier et al., 2003). Gianella and
102 Stuedlein (2017) studied the behavior of sands and silty sands treated by TDP in South Carolina,
103 proposing this technique as a suitable and potentially sustainable ground improvement alternative.
104 Significant increases in cone resistance were observed after installation, though followed by a
105 reduction in the long term. Finally, Li et al. (2018) reported a series of in-situ tests and full-scale
106 field tests to investigate the RCM compaction effects on laterally loaded piles in silts and silty sands

107 in eastern China, showing that this approach results in increase lateral resistance of the piles as well
108 as in a reduction in soil liquefaction potential.

109 The increase in penetration resistance due to the installation of the ground improvement techniques
110 described previously is generally attributed to the increase in soil density alone, erroneously
111 neglecting the influence of lateral stress. Nonetheless, it has been observed (Harada et al., 2010;
112 Salgado et al., 1997) that the potential increment of lateral pressure can go well above the normally-
113 consolidated state, thus contributing to the increase of the liquefaction resistance within the
114 improved soils. In addition, it is still uncertain how to accurately account for the composite action
115 of discrete elements and soil. Soil-cement columns or grids constructed by cement deep soil mixing,
116 jet grouting, or other methods (e.g. SC) are considered effective for mitigating liquefaction in silty
117 sands by shear reinforcement mechanism (e.g. Mitchell, 2008; Adalier and Elgamal, 2004).
118 However, recent numerical studies by Rayamajhi et al. (2014, 2016) and Green et al. (2008)
119 demonstrated that discrete columns may deform in both flexure and shear, being less effective in
120 reducing shear stresses than what shear stress compatibility implies. Investigations based on
121 vibroseis “T-Rex” and/or cross-hole tests in New Zealand and Ecuador (Wissmann et al., 2015;
122 Smith and Wissmann, 2018) provided evidence that RAP reinforced ground is significantly stiffer
123 than the untreated natural soil.

124 The level of shear stress reduction in the surrounding soil due to the in-situ installation of discrete
125 columns has still not been demonstrated by field data. Therefore, full-scale liquefaction tests in the
126 field, under controlled conditions, are important for a proper quantification of lateral stress and
127 shear stiffening phenomena. These tests will improve understanding of the behavior of the soil and
128 column composite response under conditions similar to those induced by earthquakes.

129 Previous experiences in the United States and New Zealand (e.g. Ashford et al., 2004; Wentz et al.,
130 2015; Saftner et al., 2015; Gianella and Stuedlein, 2017) show that liquefaction can be induced and
131 monitored in clean sands with controlled blasting. Some efforts have also recently focused on
132 studying the behavior of siltier deposits during blast-liquefaction tests in Italy (Amoroso et al.,

2017; Fontana et al., 2019; Passeri et al., 2018; Pesci et al., 2018). Furthermore, little research is available to demonstrate RAP effectiveness in mitigating liquefaction in sandy silts and silty sands, using blast-induced liquefaction. Nevertheless, preliminary results from a silty sandy case history in Ecuador suggest that RAP ground improvement elements installed beneath a 700 m-long bridge embankment prevented lateral spreading and settlement during the 2016, M_w 7.8 Muisne earthquake (Smith and Wissmann, 2018).

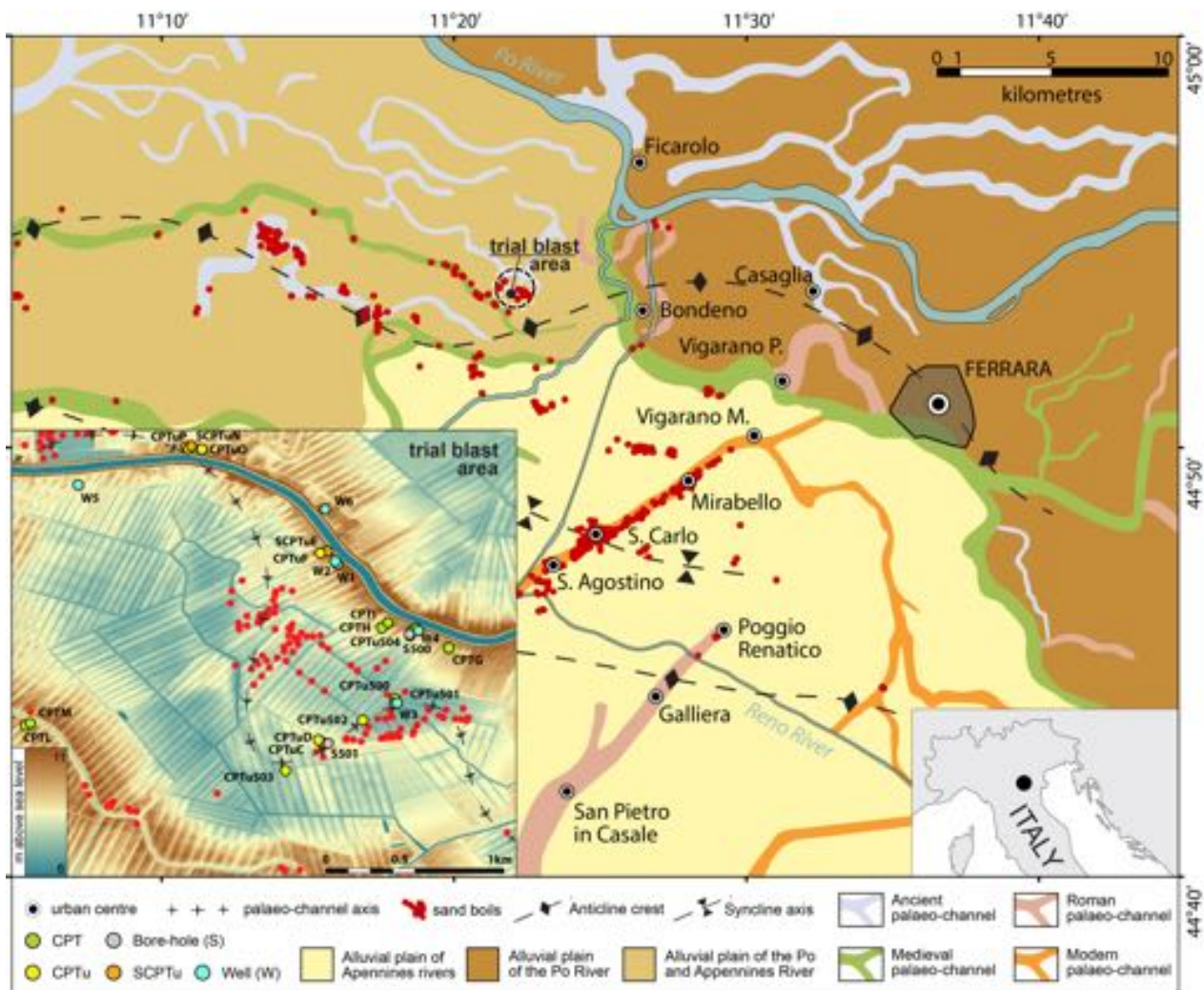
In this context, full-scale blast tests were performed at a silty sand site in Bondeno (Ferrara, Italy) where liquefaction was observed after the 2012 Emilia-Romagna earthquake (Emergeo Working Group, 2013), as preliminarily presented by Amoroso et al. (2019). Compared to previous blast experiences, the present study is based on a multidisciplinary approach, involving a team of forty researchers with expertise in the fields of geology, geophysics, geotechnical engineering and site surveying, in order to gain a comprehensive understanding of the mechanisms governing the selected engineering solution for liquefaction mitigation. Geotechnical testing, surface seismic and geoelectrical surveys were performed before and after RAP installation, as well as after blasting, to verify the effectiveness of the treatment. An array of explosive charges was detonated sequentially on improved and unimproved test areas to evaluate relative liquefaction resistance after RAP installation, monitoring excess pore pressures, settlements and accelerations. Also, four small exploratory trenches were dug to identify deformational features related to the blast tests and to characterize the fractures/conduits used by the liquefied sands during blast tests and in the 2012 earthquake. Samples of ejecta and in-situ sand were collected to characterize the soil deposits with geotechnical and/or petrographic laboratory tests. This combination of geological and geotechnical methods appears to be vital for a proper interpretation of the liquefaction process and for verifying the seismic origin of dykes (Obermeier, 1998). The paper describes the testing program and presents insights from this multidisciplinary study.

157

158 **2. Geology, geomorphology, and seismotectonic framework of the study area**

2.1. Geological setting

The blast test site area is located in the south-eastern portion of the Quaternary alluvial plain which extends between the southern Alps and the northern Apennines. This plain is one of the deepest alluvial plain in Europe, though the exact depth of the seismic bedrock and the relevant seismic-wave properties are still a matter of debate among researchers (Molinari et al., 2015). The test site lies on the buried external portions of the Apennine chain, consisting of seismically active fault-fold structures (Toscani et al., 2009). The sedimentary units involved in the experiment accumulated during the late Pleistocene and Holocene periods, and show significant lateral variability in thickness (Minarelli et al., 2016). The latest Pleistocene unit is part of a depositional cycle typically referred to as Villa Verrucchio Subsynthem (AES7), whereas the Holocene sediments pertain to the Ravenna Subsynthem (AES8). Several generations of fluvial channel deposits were fed from the south by the Apennine streams and from the west by the Po River (Fig. 1).



171

172 Fig. 1. Map of the paleochannel bodies (modified after Stefani et al., 2018), of the surface
 173 manifestations of liquefaction following the 2012 Emilia-Romagna earthquake (Emergeo Working
 174 Group, 2013) and of the location of the blast area. The traces of the main anticline crest and
 175 syncline axis of the buried tectonic belt are also depicted. The lower-left corner shows the
 176 geomorphological features from LIDAR map together with the available investigations and the
 177 2012 sand boils.

178

179 2.2. Seismic activity and effects

180 The area has a seismic history of low- to moderate-magnitude events. The most relevant past event
 181 is the VIII MCS (moment magnitude M_w 5.5) 1570 earthquake that struck the area of Ferrara,
 182 causing liquefaction phenomena, open fractures and changes in channel water flows (Caputo et al.,

183 2016). In May 2012, a seismic sequence affected the area with two main shocks (Pondrelli et al.,
184 2012). The first occurred on May 20th (M_w 6.1), with an epicenter at about 15 km to the south-west
185 of the test site, followed by aftershocks up to M_w 5.1. The second main seismic event took place on
186 May 29th (M_w 5.9), with an epicenter located at about 24 km to the south-west of the test site. The
187 highest peak ground accelerations (*PGA*) recorded at nearby strong-motion stations located in the
188 epicentral area turned out to be approximately 0.3g and 0.9g, for the horizontal and vertical
189 components, respectively (Luzi et al., 2013). Both main shocks induced important secondary effects
190 at the surface, such as widespread liquefaction, sand boils (Fig. 1) and ground failures, together
191 with lateral spreading and differential settlements. Sand boils and liquefaction manifestations
192 occurred mainly along paleochannel deposits (Fig. 1).

193

194 **2.3. Geomorphological framework**

195 A strong link between the geographic distribution of the fluvial sand deposits and the location of
196 liquefaction events was observed for the 2012 seismic crisis (e.g. Papathanassiou et al., 2015;
197 Caputo et al., 2016) using satellite images and high-resolution LIDAR topographic models (Civico
198 et al., 2015). The detected geomorphological features were also documented by the comprehensive
199 database of subsurface investigations collected for the ongoing seismic microzonation (Fig. 1) and
200 by other studies (Amoroso et al., 2020; Tonni et al., 2015).

201 The selected test site, which experienced the occurrence of a large number of sand boils (Fig. 1)
202 during the 2012 seismic sequence (Emergeo Working Group, 2013), is located above a meander
203 point bar structure. This meander morphology is partially confined by younger higher fluvial ridges
204 bordering the test area in the south and the north (Fig. 1) and forming an interfluvial depression.

205

206 **2.4. Stratigraphic organization**

207 The fluvial sediments at the test site belong to three superimposed units, related to different
208 depositional environments and chronological intervals (Figs. 1 and 4):

(a) the lower unit consists of fluvial medium-grained sands and silty sands, deposited during the late glacial maximum (Pleistocene) into a braided river channel system (upper portion of AES7 unit). This unit is about 20 m-thick topped by a regional paleosoil surface, overlain floodplain fine-grained sediments. At the test site, the top of this unit corresponds to the erosive base of a Holocene fluvial channel sand body;

(b) the middle unit is formed by fluvial sandy silts, laterally grading into argillaceous sediments. This unit is approximately 9 m-thick (AES8 unit, Holocene). The interpretation of satellite images and topographic data, coupled with information obtained from subsurface logs, suggests that the sand accumulated into a meandering channel of the Po River. At the test site, this unit is buried at a shallow depth. The liquefaction induced by the blast test largely took place within this unit;

(c) the upper unit comprises fluvial clays and silts (3 m-thick) forming the uppermost part of the AES8 unit, deposited during the final infilling of the fluvial channel, probably recording influxes from Apennine-derived rivers.

3. Description of the field activities

The blast tests activities were conducted over a period of one year (November 2017-October 2018), as listed in Table 1.

Table 1. Activities associated with blast tests at Bondeno site.

Phase	Activity	Period
I	Preliminary investigations for site selection	November 2017-January 2018
II	Geotechnical and geophysical tests for characterization of the test site	February-March 2018
III	RAP column installation	March-April 2018
IV	Geotechnical and geophysical tests one month after RAP installation	April-May 2018
V	Installation of blast holes, profilometers, accelerometers, pore pressure transducers	May 2018
VI	Blast tests	4 June 2018
VII	Geotechnical and geophysical tests soon after blast tests	June 2018
VIII	Geotechnical and geophysical tests one month and a half to two months after blast tests	July-August 2018
IX	Geological, geotechnical and geophysical tests three to four months after blast tests	September-October 2018

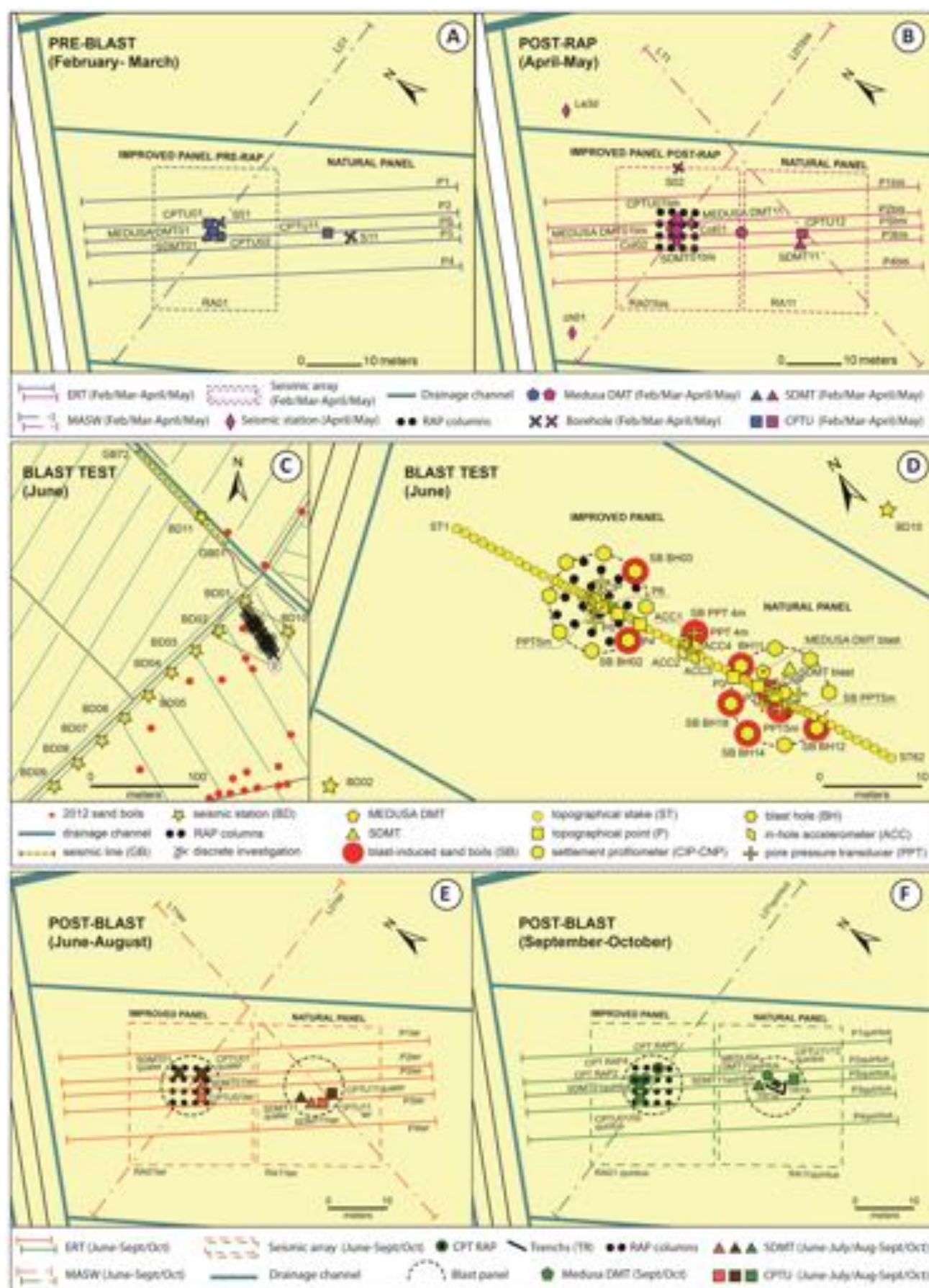
228 From November 2017 to January 2018, preliminary investigations were aimed at identifying the
229 most suitable test site. This choice was guided by the need to select a shallow liquefiable layer of
230 silty sands, also taking into account the previously mentioned geomorphological considerations and
231 2012 liquefaction evidences. Furthermore, the site was located at a distance from buildings and
232 human activities of this area in order to minimize the effect of vibrations generated by the
233 detonation.

234

235 **3.1. Pre-blast activities**

236 **3.1.1. Pre-RAP investigations**

237 From February to March 2018 an intensive geotechnical and geophysical campaign was carried out
238 in order to achieve a detailed characterization of the upper 20 m of the subsoil, also useful for the
239 design of the RAP columns and the blast tests. These surveys allowed identifying a relatively
240 homogeneous area (60 m x 40 m), where two blast panels - one for testing the natural soil (Natural
241 Panel, NP) and one for the improved soil (Improved Panel, IP) - were eventually placed (Figs. 2a
242 and 2b). Later investigations were all concentrated in these two relatively small circular areas
243 spaced 20 m apart, each having a diameter of 10 m. The geotechnical investigations, pushed to
244 approximately 15 to 20 m in depth, consisted of: (i) two boreholes, one in the IP and one in the NP,
245 along with standard penetration testing (SPT) and disturbed soil sampling for grain size distribution
246 analyses, determination of Atterberg limits, petrographic analyses and radiocarbon dating; (ii) two
247 piezocone (CPTU) tests, one in the IP and one in the NP; (iii) one seismic dilatometer (SDMT) test
248 in the IP. The geophysical surveys consisted of: (i) five electrical resistivity tomography (ERT)
249 alignments, spaced at 2 to 5 m and 63 m long (64 electrodes for each line), crossing the IP and the
250 NP; (ii) one active P-wave and S-wave tomography, 71 m long, performed using firstly 72 vertical
251 geophones and secondly 72 horizontal geophones along the same line; and (iii) one passive 2D-
252 rectangular array (24 m x 21 m) using 72 P-wave geophones spaced at 3 m, and centered in the IP.



254 Fig. 2. Map of the investigations at the test site carried out pre-blast in February-March 2018 (a),
255 post-RAP in April-May 2018 (b), during blast at small (c) and large (d) scale, post-blast in June-
256 July-August 2018 (e) and in September-October 2018 (f).

257

258 Grain size analyses were carried out using a Mastersizer 3000 particle size. Compositional analyses
259 under transmitted light microscopy were performed on the 0.125–0.250 mm fraction, according to
260 the Gazzi-Dickinson method, designed to minimize the dependence of the analysis on the grain-size
261 (Fontana et al., 2015).

262 Prior to RAP installation, a 0.5 m-thick, geosynthetic-reinforced, gravel platform was set up to
263 allow the access of the RAP installation equipment machinery. Moreover, an additional CPTU was
264 performed to check the IP homogeneity, and a SDMT was also performed within the NP.

265

266 **3.1.2. RAP installation**

267 Between the end of March and the beginning of April 2018, a 4x4 quadrangular grid (2 m center-to-
268 center spacing) of RAP columns, each 9.5 m long, was built (Fig. 2). The final diameter of each pier
269 was 0.5 m with an associated area replacement ratio, defined as the ratio of the pier area to the
270 tributary soil area surrounding the pier, equal to 5%. Because of construction issues, the last column
271 of the third line was limited to only 5.5 m depth. For quality control of the ground improvement
272 work, ten RAPs were subjected to aggregate flow rate tests and crowd stabilization tests in order to
273 evaluate the pier gravel volume and to measure the column stiffness, respectively. These tests
274 revealed a reduced effectiveness of the construction procedure for the upper-left piers.

275 The RAP elements were constructed using a displacement technique with an excavator mounted
276 mobile ram base machine fitted with a high frequency (30 to 40 Hz) vertically oscillating hammer
277 as illustrated in Fig. 3.

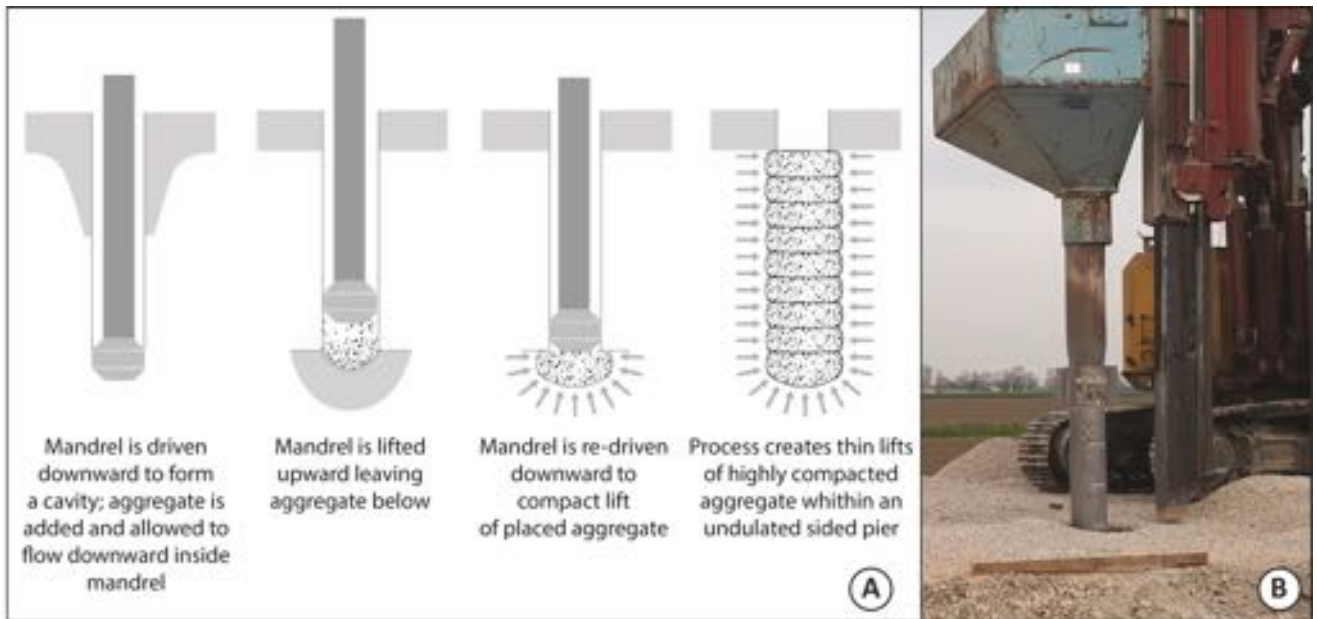


Fig. 3. (a) RAP column installation scheme with vibratory hammer and hopper/mandrel for gravel installation (Wissmann et al., 2015); (b) RAP installation at Bondeno test site.

The base machine drives a 300 mm outside diameter open-ended pipe mandrel fitted with a unique specially-designed 360 mm diameter tamper foot into the ground. Proprietary internal restrictor elements prevent soil from entering the mandrel during driving and serve as an internal compaction surface during tamping. After driving to the designed depth, the hollow mandrel serves as a conduit for aggregate placement. Placed inside, the aggregate flows to the bottom of the mandrel. The tamper foot and mandrel are then raised approximately 0.9 m and then driven back down 0.6 m, forming a 0.3 m-thick compacted lift. Compaction is achieved through static down force and dynamic vertical ramming from the hammer combined with the confinement of the tamper's restrictor elements. The process densifies aggregate vertically and the beveled tamper foot forces aggregate laterally into cavity sidewalls. Crushed gravel (typically graded at 10 to 40 mm in particle size) is fed through the mandrel from a top mounted hopper and compacted in the displaced cavities to create approximately a 0.5 m-diameter, dense, stiff, aggregate pier element. The construction methodology has been described in detail by Saftner et al. (2018).

3.1.3. Post-RAP investigations

At the end of April 2018 supplementary geotechnical tests were carried out in the middle of four piers (Fig. 2b) and pushed to a maximum depth of 15 m, in order to evaluate the RAP effect on soil response one month after construction. DMT soundings were performed using a new device, the Medusa DMT, that is a combination of the flat dilatometer with hydraulic automation and a measuring system for autonomously performing DMT tests (Marchetti et al., 2019).

At the beginning of May 2018, the temporary gravel platform was removed to allow additional geophysical surveys with the same configuration as the original investigation (Fig. 2b): (i) five ERT alignments; (ii) two active P-wave and S-wave tomographies, one in the IP and one in the NP; (iii) two passive 2D-rectangular arrays, one centered in the IP and one centered in the NP; and (iv) four surface seismic stations, equipped with three-components Lennartz-5s velocimeter, two in the treated area and two in the natural soil.

3.2. Blast activities

In May 2018, blast holes, profilometers, accelerometers, pore pressure transducers, seismic DMT and Medusa DMT equipment were installed in the ground. Topographical reference points, seismic stations and geophones were placed on the surface in preparation for the blast tests that took place on June 4th, 2018 (Figs. 2c and 2d). Locations of the instrumentation relative to the blast holes for each panel are shown in Fig. 2d.

Eight blast holes (BH), 7 m deep and equally distributed along a 5 m-radius ring, were drilled in each panel. Charges were located in each BH at 3.5 m (0.5 kg) and 6.5 m (2.0 kg) within the potentially liquefiable layer. This soil layer was detected between 3 and 8 m depth according to a preliminary assessment of liquefaction susceptibility, that considered a design earthquake for a 475 years return period ($M_w = 6.14$ and $PGA = 0.22g$, Amoroso et al., 2019).

At the center of each panel, a profilometer (CNP for the natural panel and CIP for the improved panel) was anchored at 15 m depth to record the settlement vs. depth profile. In fact, previous

322 experiences worldwide (e.g. Amoroso et al., 2017; Gianella and Stuedlein, 2017; Finno et al., 2016)
323 provided evidence of a bowl shaped displacement surface following blasting. Furthermore, from the
324 previous blast experiment carried out in a site of the Po River valley, it was observed that
325 settlements in the circular blasting area were similar to liquefaction-induced vertical displacements
326 predicted for a M_w 7.5 earthquake in the same depth interval (Amoroso et al., 2017).

327 To estimate blast-induced shear strains and shear stresses, four in-hole 200g triaxial
328 microelectromechanical (MEMS) accelerometers (ACC) were located at approximately midway
329 between the two panels (i.e. about 10 m from CNP and CIP), using a 1 m-squared configuration
330 between 3.5 and 4.5 m deep and recorded at a sampling rate of 1000 Hz. Pore pressure transducers
331 (PPT) were installed from 4 to 9 m at each meter of depth, within the liquefiable layer (1 or 2 m
332 distance from the center of each panel) to measure the generation and subsequent dissipation of the
333 excess pore pressures induced by the blasts in the silty sand deposits of both panels, at a sampling
334 rate of 100 Hz. An additional PPT was set up at an average depth of 4 m in the middle of the
335 accelerometer array to study the non-linear soil response induced by the blast-liquefaction, coupling
336 the shear strains with the excess pore pressures. A SDMT and a Medusa DMT were finally installed
337 at 6.1 m deep in the natural panel to monitor the variation of shear wave velocity with excess pore
338 pressure following the blasts.

339 Six survey rods (P) were located within the NP and the IP and an alignment of sixty-two survey
340 stakes (ST) crossing both panels was set up to record the vertical ground surface settlements over
341 time after the blasts and to integrate with the profilometer data, Terrestrial Laser Scanning (TLS),
342 and Structure from Motion (SfM) aerial photogrammetry. A line of seventy-two P-wave geophones
343 (GB, 4.5 Hz) was installed at an average distance of 100 m from the blast area, while eleven surface
344 seismic stations (BD), each of them composed of a velocimeter (Lennartz-5s) and an accelerometer
345 (Episensor-1s), were located along a Y-shaped configuration, having the closest and the farthest
346 stations at 25 and 250 m, respectively (Fig. 2c), to record the particle motion with distance and to
347 verify the level of vibration generated by the detonation.

Explosives were detonated on June 4th, with a microdelay of 1 second between subsequent charges and starting the detonation from the bottom (6.5 m deep) to the upper level (3.5 m deep). The blasts of the two panels were designed separately (i.e. blast #1 for the NP and blast #2 for the IP) to limit effects of superposition and consequently to study the effect of the blast-induced liquefaction on the IP and the NP separately.

Surface movements induced by underground explosions and liquefaction effects were observed by means of TLS and SfM surveys performed before and after each blast test providing and comparing multi-temporal Digital Terrain Models (DTMs). Unmanned Aerial Systems (UAS) equipped with DJI FC6310 and DJI FC350 cameras and a Teledyne Polaris scanner were used. The results from TLS dense point clouds, characterized by a mean 5 mm sampling step, provide a complete description of subsidence rates in the area following liquefaction and pore pressure dissipation.

3.3. Post-blast activities

Three post-blast investigations were performed in June, July-August and September-October 2018 (Figs. 2e and 2f), with the aim of comparing the variation with time of the geotechnical and geophysical parameters before and after the blast tests in both panels.

Two piezocone and two seismic dilatometer tests were carried out up to 15 m deep, in the IP and the NP soon after the blast tests. Moreover, in June 2018 ERT surveys and active and passive geophysical surveys were performed using the same configuration of the previous investigations shown in Fig. 2e.

One month and a half to two months after the blast tests, an additional in-situ testing campaign was repeated: two CPTUs and two SDMTs were performed, up to 15 m deep, between piers and within the untreated area, as shown in Fig. 2e.

Finally, three to four months after blasting, the last geotechnical and geophysical tests were carried out, as reported in Fig. 2f. As for the previous investigations, CPTUs, SDMTs and Medusa DMTs were performed in the IP and the NP, pushing tests to a maximum depth of 15 m. Moreover, three

374 mechanical cone penetration tests were performed at the center of RAP piers (CPT RAP) to a depth
375 of approximately 11 m. In September-October 2018 ERT, active and passive geophysical surveys
376 were repeated again using the same configuration of the previous investigations.
377 At the conclusion of the experimental activities, four small exploratory trenches were dug across the
378 liquefaction-induced sand boils within the natural panel (Fig. 2f). The excavations were performed
379 to better understand the blast-induced liquefaction mechanism but also to identify and characterize
380 the fractures/conduits used by the liquefied sands in the 2012 earthquake (Amoroso et al., 2017) and
381 possibly during older events (De Martini et al., 2012; Caputo et al., 2016). Moreover, sand samples
382 were collected from the fractures as well as from the surface (sand boils) in order to study the
383 variability in grain size potentially related to the liquefaction process and to the liquefied sand paths
384 (Fontana et al., 2019).

385

386 **4. Main geotechnical features from the pre-blast investigations**

387 The interpretation of all the geotechnical and geophysical investigations performed in both panels
388 (IP, NP) prior to improvement was used to define a representative stratigraphic model of the natural
389 subsoil (Fig. 4a). The identified soil units are listed below and classified in terms of the Unified Soil
390 Classification System (USCS), according to ASTM D2487-11 (2011):

- 391 (i) top soil (CH) from the ground surface to 0.8 m;
- 392 (ii) clays and silts (CL) from 0.8 to 3.4 m;
- 393 (iii) silty sands (SM) from 3.4 to 12.6 m (paleochannel of the Po River);
- 394 (iv) sandy silts (ML) from 12.6 to 13.4 m (well-drained interfluvial deposits);
- 395 (v) sands and silty sands (SM-SP) from 13.4 to 15.6 m (glacial braided Po River deposits).

396 The silty sands (SM) and sandy silts (ML) have laterally a variable thickness due to their channel-
397 filling nature. In this respect, the ML layer can vary in depth between 11.70 and 13.40 m, and have
398 a minimum thickness of approximately 0.5 m.

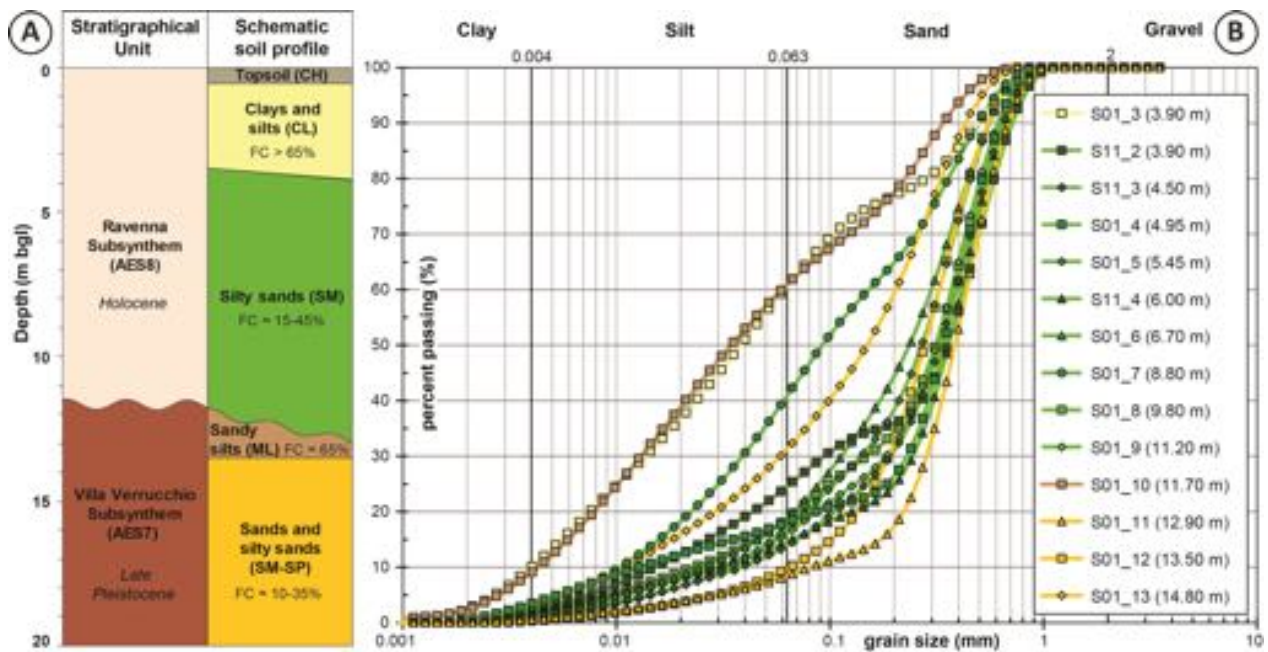


Fig. 4. Average subsoil profile at the test site and stratigraphic units (a) and grain size analyses (b).

Fig. 4b shows the results of the grain size analyses performed on the disturbed samples from S01 and S11 boreholes. The analyzed samples range from silty sands to silts with a variable amount of sand and clay. The majority of samples fits in a relatively narrow range, predominantly made up of fine sands; the content of silt is on average less than 25% and clay is < 5%. A higher percentage of fine sediments can be found in the shallowest sands (3.9 m depth) or in thin lenses detected at 8.8, 11.7 and 14.8 m depth. In particular, Fig. 4 shows that the SM layer has a fine content $FC \approx 15$ -45%, while $FC \approx 65\%$ for the ML layer and $FC \approx 10$ -35% for the SM-SP layer.

Sands from cores S01 and S11 have a quartz-feldspar rich composition and are made up of quartz, feldspars and subordinate lithic fragments. Siliciclastic lithics include low-grade metamorphic rocks, shales and spillite and carbonate lithic. Crystals of muscovite, chlorite and biotite are also present as well as heavy minerals. The composition of the sands show a clear affinity with sands from the Po River.

With reference to the defined stratigraphic model, Fig. 5 shows the soil response prior to RAP installation in terms of corrected cone resistance (q_t) from CPTU test, horizontal stress index (K_D) and shear wave velocity (V_S) from the SDMT test. The variation of q_t and K_D profiles with depth

looks related to the geologic depositional environment. Below the fine-grained units detected in the upper 3.4 m, the paleochannel of the Po River (from 3.4 to 12 m) is characterized by different q_t and K_D values when compared with glacial braided Po River deposits (below 13.4 m). In contrast, the V_S increases consistently with the effective vertical stress.

Fig. 5 also provides interpretations of CPTU measurements in terms of the soil behavior type index (I_{cn}), fines content (FC) according to Robertson and Wride (1998), and relative density (D_R) computed with the correlation proposed by Jamiolkowski et al. (2003). The computed FC values appear to be generally underestimated in comparison with those obtained from laboratory tests (blue dots in Fig. 5). However, at the test site the dataset is currently too small to develop a site-specific correlation that would take into account the uncertainties related to FC - I_{cn} relationship (e.g. plasticity and mineralogy).

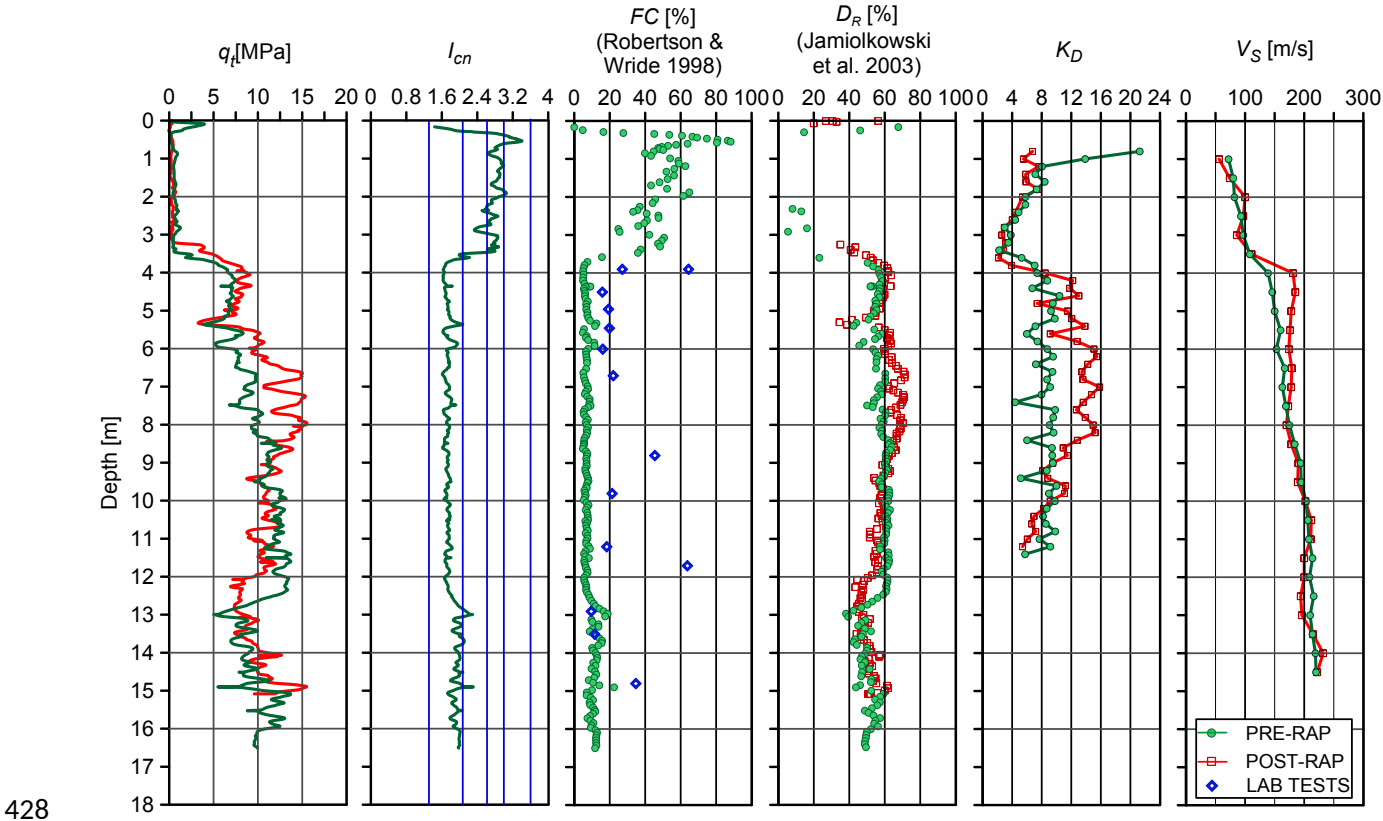


Fig. 5. CPTU and SDMT profiles pre/post RAP installation.

5. Main outcomes from the experimental activities

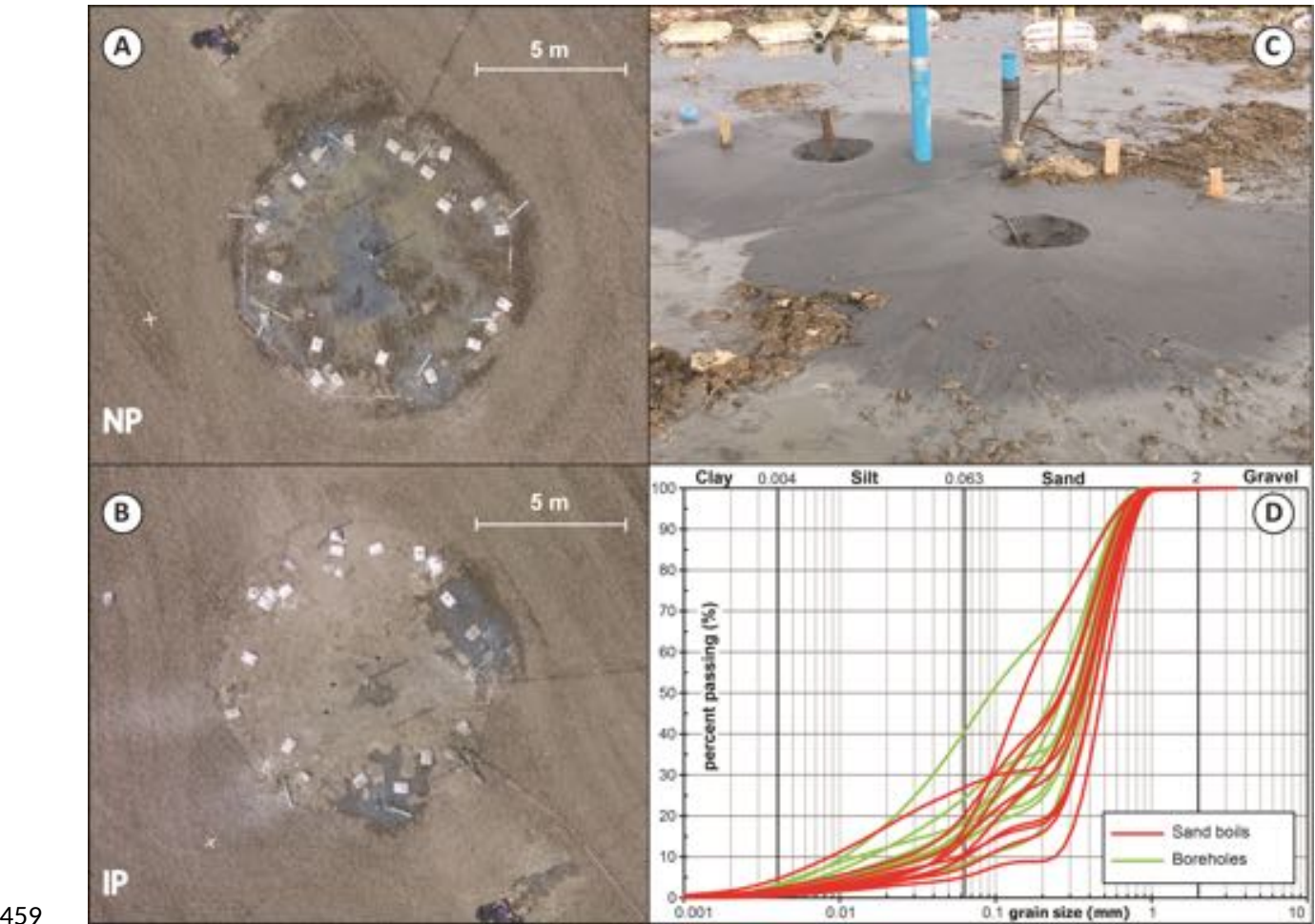
5.1. Post-RAP investigations

The site investigation performed one month after RAP column installation was helpful to understand the effectiveness of the ground improvement technique. Fig. 5 provides a comparison between field soil responses before and after treatment, in terms of both CPTU and SDMT profiles. A decrease of soil properties in the upper crust, partly due to the construction of the platform, but also to the low confinement induced by RAP installation and the seasonal variations in water content caused by fluctuation of the GWT from 1.5 m (February 2018) to 0.8 m (April 2018), is observed. Conversely, the layer between 3.4 and 9.5 m shows an increase in resistance and stiffness due to the installation of the piers. Unlike clean sands studied in New Zealand (e.g. Wissmann et al., 2015, Vautherin et al., 2017), in this case no improvement was detected in the silty sands below the toe of piers (Fig. 5). Looking in detail at the in-situ test data between 3.5 and 5.5 m depths, q_t and K_D increase on average from 7 to 8 MPa, and from 7-9 to 12, respectively. This trend is further confirmed in the underlying layer, between 5.5 and 9.5 m, where the natural soil is characterized by $q_t \approx 8-10$ MPa and $K_D \approx 7-9$, and the treated soil assumes values of $q_t \approx 10-14$ kPa and $K_D \approx 13-15$. Moreover, from 3.5 to 5.5 m in depth, the CPTU-based estimates of D_R shows a minor increase after pier installation, whereas a more significant increase is observed at 5.5-9.5 m (i.e. from approximately 60 to 70%). In contrast, V_S measurements show a limited improvement between 4 and 7 m depth, from 140-165 to 175-185 m/s, and remain constant below 7 m (Fig. 5). This tendency may be related to the decrease in vertical effective stress with some disturbance to the soil structure (e.g. Mitchell and Solimar, 1984), for RAP installation.

5.2. Blast test effects

Figs. 6a and 6b show the results of the aerial SfM survey after both blasts. It can be easily observed that liquefaction was induced in the NP, as clearly indicated by the widespread sand boil evidence in this location (see also Fig. 2d). In contrast, only minor liquefaction traces are observed within the

457 IP, mainly near the edge of the blast ring. These limited sand boils are, however, outside the limits
458 of the RAP group and likely developed in unimproved soils in this area.



460 Fig. 6. SfM point cloud of surveyed area showing liquefaction-induced sand boils after blast #1 in
461 the NP (a) and blast #2 in the IP (b). Detail of the sand boils in the NP (c); grain size distributions of
462 the sand boils (in red) compared with sands from the boreholes (in green) (d).

463
464 Fig. 6c documents the sand boils induced by the blast in the NP after blast #1. Grain size
465 distribution analyses on soil samples collected from the sand boils (green curves in Fig. 6d) detected
466 medium-grained sands with a fines content varying between 6 and 28%. Compared to grain size
467 characteristics of the source beds (i.e. SM layer, red curves in Fig. 6d), a selective loss of fines can
468 be appreciated in the ejected sediments forming the sand boils, thus indicating that the liquefaction

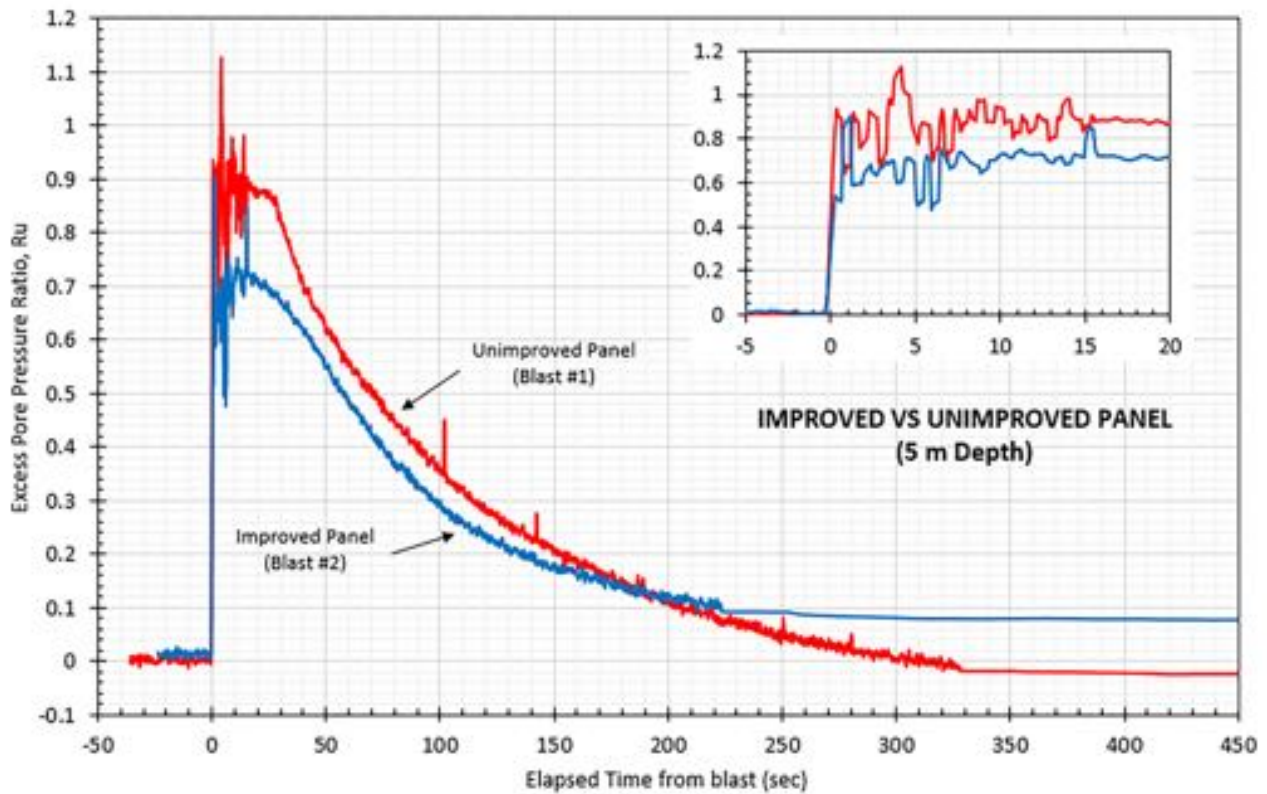
469 process appears to preferentially select the grain diameters, as previously found by Fontana et al.
470 (2019), Maurer et al. (2019) and Cubrinovski et al. (2018).

471 Pore pressures measured by the PPT were used to compute excess pore pressure ratios ($R_u =$
472 $\Delta u / \sigma'_{v0}$) in the NP and the IP, where Δu is the measured excess pore pressure and σ'_{v0} is the initial
473 vertical effective stress prior to the blasts. Soil unit weights were interpreted from the SDMT tests.

474 In the NP, R_u values reached 1.0, indicating liquefaction, from a depth of 4 to 9 m. Plots of R_u
475 versus time after blasts are presented in Fig. 7 for transducers at a depth of 5 m in the IP and the NP.

476 In the NP, the blast sequence produced R_u values near 1.0 which persisted for 15 to 30 seconds (see
477 the zoom in Fig. 7) and then dissipated to near static levels in about 4 minutes. In the IP, peak R_u
478 values were somewhat lower ($R_u = 0.75$) than in the NP, but dissipated at a similar rate.

479 Settlement profilometers indicated that liquefaction, and subsequent reconsolidation, occurred
480 within a zone from about 3 to 11 m below the ground surface which is generally consistent with the
481 expected zone of liquefiable sediments. In the NP, volumetric strains were consistent with what
482 would be predicted by Zhang et al. (2002) if a M_w 7.5 earthquake had produced liquefaction from 3
483 to 11 m with a factor of safety of about 0.9. Volumetric strains in the same depth interval for the IP
484 were about 20% of those measured for the NP, despite excess pore water pressure values that
485 resulted in R_u values of 0.7 to 0.9.



486

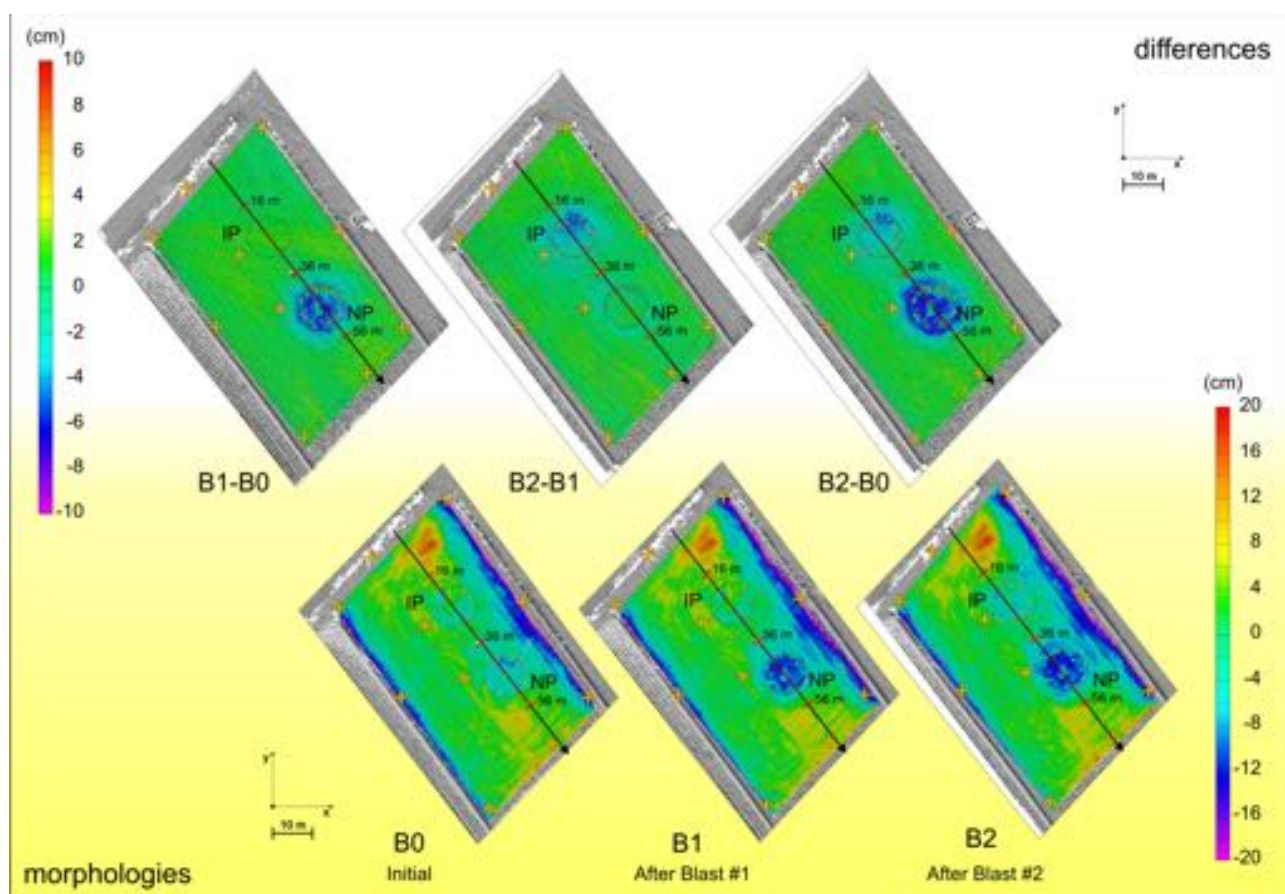
487 Fig. 7. Comparison of measured excess pore pressure vs. time curves for the IP and the NP at a
 488 depth of 5 m below the ground surface. For both panels the PPTs recorded at a sampling rate of 100
 489 Hz and the R_u values were smoothed using a 100 point running average. This was done so that the
 490 residual excess pore pressure would not be obscured by the transient pressure spikes.

491

492 Fig. 8 shows color settlement contour maps obtained by comparing the TLS-based multi-temporal
 493 models with the terrain morphology maps. In the NP, after blast #1 there is clear subsidence of the
 494 area within the explosive charges, with a widely distributed settlement of about 6-8 cm. In contrast,
 495 after blast #2 only a few small sectors of the IP experienced settlement with an average of 2 cm
 496 (locally maximum 4-5 cm). For both blast tests, settlements were mainly delimited within about 10
 497 m from the centers of the blast areas.

498 All topographical surveys indicate that settlements within the NP were on average between 7 and 10
 499 cm, after both blasts. In contrast, settlements within the IP were between 2 and 5 cm. Liquefaction
 500 induced settlements in the NP would likely be excessive for many structures, whereas the reduced

501 settlements in the IP would likely be tolerable. The mechanisms responsible for the reduced
 502 settlement in the panel treated with RAP columns may be related to soil densification and increased
 503 lateral stress, but soil-pier interactions may also play a role. Due to the whole test setup the bearing
 504 capacity was not evaluated, even though it is another important issue within liquefaction evaluation
 505 criteria.



506
 507 Fig. 8. Difference maps between TLS-based point clouds (upper panels), where BN-BM means N-
 508 th point cloud compared with respect to the M-th one, and morphological maps (lower panels).

509
 510 Fig. 9 shows the SDMT results recorded in the NP during both blasts. Soon after the blast #1, the
 511 SDMT data show a shear wave velocity decrease to about 30% of its pre-blast value ($V_S \approx 49$ m/s
 512 versus $V_S \approx 152$ m/s), while it took a few minutes to recover to approximately its initial value. For
 513 blast #2, since the SDMT modulus was still installed in the NP, a smaller decrease of shear wave
 514 velocity is observed, equal to approximately 5% of its pre-blast value ($V_S \approx 141$ m/s in place of $V_S \approx$

149 m/s), associated with a much faster recovery to its initial value. These results are consistent with other previous experiences (e.g. Rollins et al., 2004; Mahvelati et al., 2016). Blast-induced liquefaction reduces indeed the vertical effective stress and alters the soil fabric, thus causing initial losses in soil stiffness (Mitchell and Solymar, 1984). However, the dissipation of the excess pore pressure allows the soil to reconsolidate into a denser and more stable configuration (Narin van Court and Mitchell, 1994) characterized by a higher soil stiffness, as confirmed also at the Bondeno trial site by R_u and V_S data (Figs. 7 and 9).

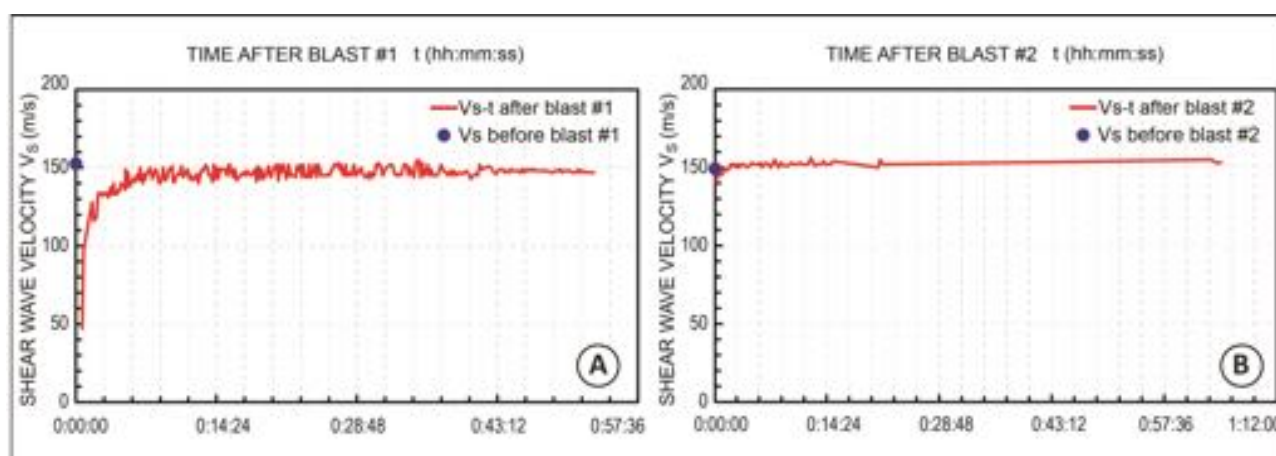
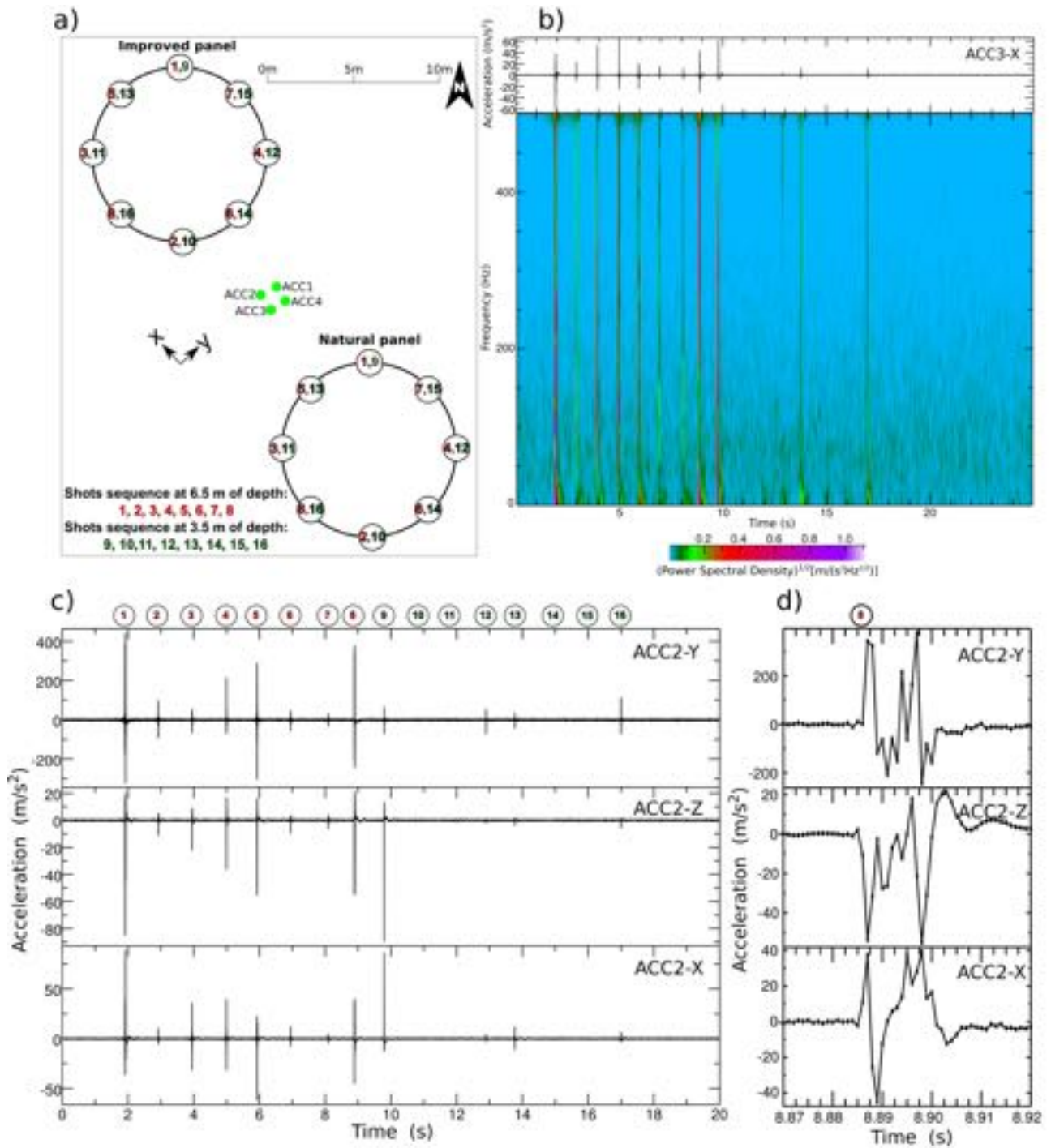


Fig. 9. Shear wave velocity data from seismic dilatometer during blasting: (a) blast #1; (b) blast #2.

All the seismic instruments installed prior to the blast tests (Figs. 2c and 2d) recorded the signals produced by both detonations. Particularly, Fig. 10 shows some examples of time-series recorded by the in-hole accelerometers. The detonations performed at 6.5 m depth produced very energetic signals that are clearly recognizable in both the time and frequency domains (Fig. 10b). Instead, the signals recorded at 3.5 m depth have generally lower amplitude, compared to the deeper ones, and, in some cases, they are difficult to detect in the recorded time-series. The seismic data produced during each blast are characterized by a very impulsive signal of short duration (about 0.02 s) and high amplitude followed by a coda having a lower amplitude and a frequency content below 25 Hz (Fig. 10b). For each detonation, the duration of the entire recorded signal does not exceed 0.4 s (Figs. 10b and 10d). The maximum peak acceleration recorded by the in-hole sensors was of about

535 45g (ACC2-Y in Fig. 10c) and 52g during blast #1 (NP) and blast #2 (IP), respectively. In both
536 cases, the maximum acceleration was recorded by the Y-component of ACC2 sensor (Figs. 10a and
537 10d). From the spectrogram (Fig. 10b), the spectral content of the signals associated to explosions
538 reach the maximum resolvable frequency (Nyquist frequency at 500 Hz) with the adopted sampling
539 rate. Nevertheless, for each shot the maximum of signal was observed during the first impulse (Fig.
540 10c) with a duration of about 0.003 s, corresponding to frequency of about 300 Hz, a value lower
541 than the Nyquist frequency.



542

543 Fig. 10. Schematic diagram illustrating the locations (and the sequences) of charges detonated in the
 544 NP and the IP with respect to the positions of the four installed accelerometers (ACC1, ACC2,
 545 ACC3, ACC4) (a); seismic traces and related spectrogram recorded during blast #1 by the X-
 546 component of ACC3 in-hole accelerometer (b); time histories of accelerations recorded during blast
 547 #1 by the three different components of ACC2 accelerometer (c); zoom of signals recorded during

548 blast #1 by the different components of ACC2 during the shot number 8. The circles on the top of
549 Figs. 10c and 10d show the number of explosions associated with the recorded signals (d).

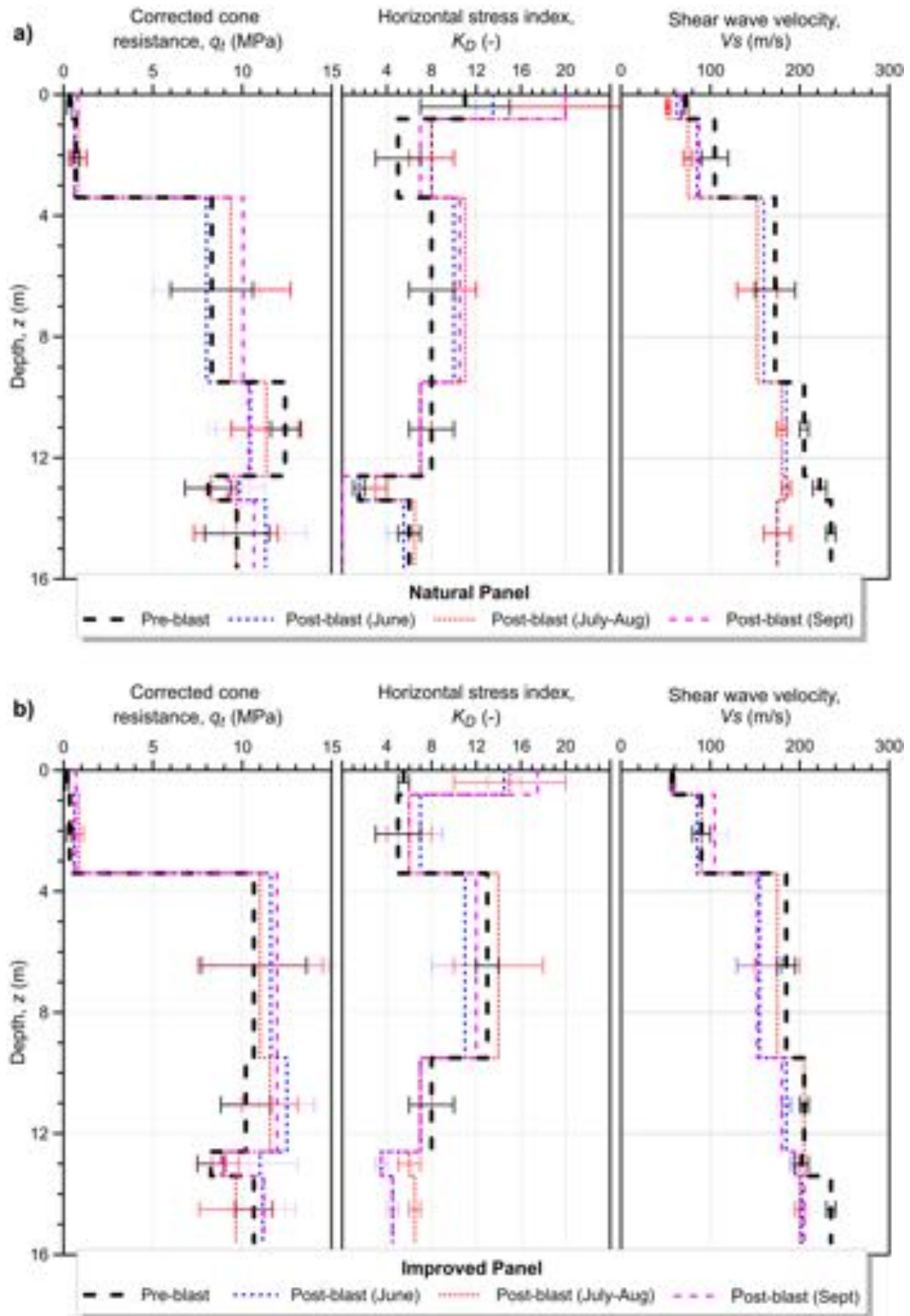
550

551 The seismic stations and the geophones permitted an estimate of the peak ground acceleration
552 (*PGA*) and peak ground velocity (*PGV*) values generated by both the blasts at distances between 20
553 and 250 m from the centers of the two panels. For blast #1, the maximum horizontal and vertical
554 *PGA* were equal to 1.2g and 1.3g, while for blast #2 the values were 0.8g and 3.6g, respectively. In
555 both cases, the blast-induced ground motion attenuated rapidly with distance and reached values
556 smaller than 0.01g at about 180 m distance. The *PGV* values provide an exponentially decreasing
557 trend with distance, consistent with other field test evidences (e.g. Gianella and Stuedlein, 2017;
558 Amoroso et al., 2017), recording ranges from 0.14 to 0.0007 m/s at 20 and 250 m distance from the
559 blast centers, respectively.

560

561 **5.3. Post-blast investigations and comparison to all previous data**

562 Fig. 11 shows the comparisons between the average profiles of q_t , K_D and V_S acquired in the pre-
563 and post-blast investigation campaigns, for both panels. Error bars are displayed in order to take
564 into account the variability of measurements within the different soil units.



565

566

567

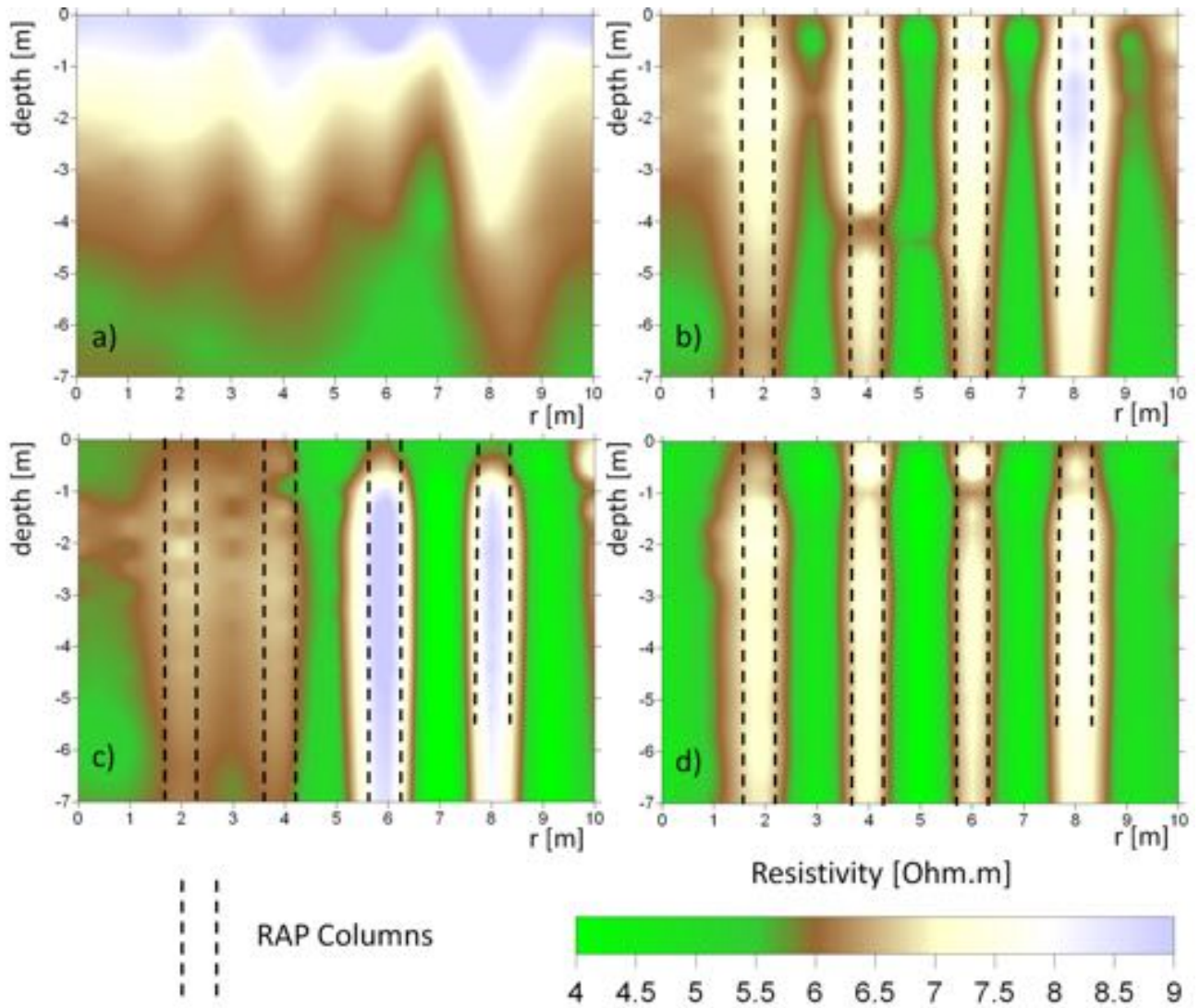
Fig. 11. Variation of the geotechnical and geophysical parameters before and after the blast test, obtained from CPTU and SDMT in the NP (a) and the IP (b).

568 With reference to the IP after blasting, the comparison of the piezocone results reveals a general
569 slight increase of the corrected cone resistance in the silty sands (SM), although the ranges reported
570 in Fig. 11b do not appear to differ significantly. Negligible changes in the q_t profiles can be
571 appreciated within the lower sands/silty sands. Similarly, the cone resistance profiles in the
572 liquefied layer (3.4-9.5 m) of the NP (Fig. 11a) slightly increase with time (from June to July-
573 August to September-October), whilst the underlying layers do not show any significant change,
574 probably as a consequence of the charge locations. It is worth observing that the horizontal spatial
575 variability of the subsoil complicates at time the direct comparison of the different CPTU
576 soundings.

577 Based on the DMT results, a few days after blasting, the horizontal stress index turned out to
578 maintain approximately its average value within the liquefiable layer of the IP (Fig. 11b),
579 confirming the effectiveness of the piers in silty sand deposits. On the other hand, a small increase
580 is detectable for the same unit in NP (Fig. 11a), consistently with CPTU measurements, probably
581 due to some densification induced by the blast-liquefaction settlements. The bottom layers do not
582 show any substantial increase. In later investigation campaigns, i.e. both in July-August and in
583 September-October, K_D values stabilized in both the blast areas, showing on average a significant
584 increase only within the liquefiable layer in the IP.

585 Finally, post-blasting time-dependent stiffness changes cannot be clearly identified in the IP (Fig.
586 11b), while an overall small V_S decrease is observed in the NP (Fig. 11a). This last finding agrees,
587 for example, with the results obtained by Mahvelati et al. (2016) in Pleistocene-aged sandy
588 deposits, whereas differs from the observations made by Passeri et al. (2018) in Holocene-aged silty
589 sands of Mirabello trial site (Emilia-Romagna, Italy). However, the Mirabello deposits are
590 relatively new Holocene sands in comparison to the deposits of the present study area. Therefore,
591 differences in geologic age and soil fabric may explain the differences in the rate and magnitude of
592 stiffness changes.

593 In Fig. 12, the main results of the geoelectric surveys executed in the different time intervals in
594 correspondence of the IP along the profile PS (see Figs. 2a, 2b, 2e, and 2f) are reported to a reliable
595 investigation depth of 7 m. The measured resistivity data generally depict a very low resistivity
596 environment (on average within 4 to 9 Ohm.m, Fig. 12a), even after the RAP construction (Fig.
597 12b). This is related both to the clayey and silty sand formations at the site and to the relevant
598 saturating water conductivity. Indeed, water samples collected in wells located in the area (Fig. 1)
599 revealed anomalously high electrical conductivity values (more than 1200 $\mu\text{S}/\text{cm}$). This condition,
600 together with the low confining pressures due to pier installation near the ground surface, has
601 influenced the imaged resistivity data, partially compromising the ability of the surveys in detecting
602 resistivity changes related to the blast effects. Particularly, inverted resistivity data were not always
603 able to image significant resistivity variations in the subsurface, particularly in the NP, contrary to
604 previous literature examples (e.g. Passeri et al., 2018). For this reason, raw apparent resistivity data
605 are presented only in the IP, since these data better reflect the local resistivity variations,
606 particularly in correspondence with the RAP columns.



607

608 Fig. 12. Apparent resistivity data imaged along the profile PS in correspondence of the IP in the
 609 different time windows of the surveys: natural soil (a); treated soil before blast (b); treated soil after
 610 blast – June (c); treated soil after blast – September (d).

611

612 Indeed in the IP the comparison of resistivity distribution imaged before and after the RAP
 613 installation (Figs. 12a and 12b) satisfactorily defines the subsoil modifications related to the
 614 installation of the gravel columns (black dashed lines in Figs. 12b, 12c and 12d). The four RAPs
 615 intercepted by the survey line are indeed well depicted in the resistivity section showing a relatively
 616 higher resistivity with respect to the natural soil. The last column of the section is known to be
 617 driven only to 5.5 m depth. Nevertheless, apparent resistivity data also show a partial increase in
 618 resistivity at greater depths probably due to compaction of the subsoil following tamping. The first

619 two piers along the section appear instead to be less homogeneous, as independently confirmed by
620 quality control tests performed during their construction (Fig. 12b). After the blast testing the same
621 first two piers along the section show a more significant resistivity reduction (Fig. 12c), which
622 makes them less evident with respect to the surrounding soil. This effect could be related to
623 increased water pressure in this zone of the IP and to partial column modifications after the blast
624 which could have compromised RAP column resistance, given also their initial reduced stiffness. In
625 this same zone of the IP, increased settlements after the blast have been depicted (Fig. 8)
626 corroborating the geophysical evidence. Nevertheless, the apparent RAP column modifications do
627 not appear to be permanent because the columns are again correctly imaged in the resistivity section
628 acquired four months after the blast (Fig. 12d). Notwithstanding the difficult environment in terms
629 of resistivity distribution, the geophysical surveys proved effective in imaging the variations
630 induced by the blast tests within the RAP columns and can be suggested as a potential monitoring
631 system.

632 Three trenches were excavated in the N350°-N355° direction (TR1a-c-d in Fig. 13a) and one in the
633 transverse N65° direction (TR1b in Fig. 13a). The geometrical arrangement of the trenches made it
634 possible to obtain detailed information on the sand boil genesis and on the previous
635 fractures/conduits used by the liquefied sands in the 2012 earthquake. Particularly, the main sand
636 boils developed during the blast tests shown in Fig. 6c reached the surface through the pore pressure
637 transducer hole (PPT5, Figs. 13b and 13c). Evidence of liquefied sand ejected toward the surface
638 was also found along the external part of the profilometer (CNP, Fig. 13d). This sand was also
639 observed filling a sub-horizontal fracture marking a stratigraphic contact (yellow flags in Fig. 13b)
640 between a silty clay, with sparse pebbles and a few charcoals (stratigraphic level 1 in Fig. 13b), and
641 an oxidized silty clay (stratigraphic level 2 in Figs. 13b and 13c). Evidence from the 2012
642 liquefaction (Figs. 13e and 13f) was also found in a 8 cm thick sand layer with a sharp basal contact
643 on the vegetated surface at the time of the earthquake (Figs. 13e and 13f). The 2012 liquefied sand
644 utilized an almost vertical thin fracture, visible to a depth of 1.5 m to reach the surface (Fig. 13g). A

645 light grey clayey silt layer at the bottom of the trench (stratigraphic level 3 in Fig. 13c) was also
 646 observed, and provisionally recognized as one of the impermeable deposits over the liquefiable
 647 sand. The ejection of sand during the blast test largely utilized pre-existing artificial paths (PPT5
 648 and CNP) and the weak stratigraphic contact between level 1 and 2.



650 Fig. 13. Geometrical arrangement of the trenches (a); details of the most significant features
 651 exposed in the walls. Sand boils from the blast test (b) were generated by sand moving upward
 652 using the PPT5 pore pressure transducer, colored flags in (c), and the external part of the CNP
 653 profilometer (d) as conduits. Sand from CNP moved sub-horizontally, as shown by yellow flags, in
 654 (b). The white dashed circle in (f) indicates the remnants of the vegetation at the ground surface,
 655 covered by the 2012 sand blow (bottom of the blow marked by colored flags in e, f). Details of the
 656 2012 vertical path (colored flags) developed along a thin fracture in (g).

658 6. Conclusions

659 Full-scale blast-induced liquefaction tests (Bondeno, Italy) made it possible to evaluate the
660 effectiveness of Rammed Aggregate Pier® (RAP) treatment in mitigating liquefaction hazards in
661 silty sands. A multidisciplinary approach was used to increase the understanding obtained from the
662 inter-related methods used to document blast-induced liquefaction behavior. The tests were
663 performed on treated and untreated panels at a test site where sand boils indicated liquefaction
664 during the 2012 M_w 6.1 Emilia-Romagna earthquake.

665 The controlled blasting experiment induced liquefaction in the natural panel (NP) consisting of
666 untreated silty sands ($FC \approx 15\text{-}45\%$) and produced surface settlements of 7 to 10 cm. Numerous
667 sand boils were induced and volumetric strains within the liquefied layers were similar to those that
668 would be expected from earthquake-induced liquefaction, in agreement with previous blast
669 experiments. Grain size distribution curves of the induced sand boils confirmed a selective loss of
670 fines relative to the source beds in-situ (paleochannel of the Po River), in agreement with previous
671 blast experiments and earthquake events. In-hole accelerometers were able to record maximum
672 peak accelerations equal to 45g and 52g, and further analysis will be performed to estimate the
673 blast-induced shear stress and shear strain.

674 Within the improved panel (IP), excess pore pressure ratios were lower than in the untreated panel,
675 but still greater than 75%. Despite these relatively high R_u values, the measured settlements (20 to
676 50 mm) were significantly lower than in the untreated natural panel, as confirmed by topographical
677 surveys and geotechnical monitoring. In addition, sand boil formation was strongly reduced.
678 Therefore, RAP treatment resulted in reducing liquefaction-induced settlements to acceptable levels
679 for many structures in comparison with the untreated natural soil. The site investigations performed
680 after blasting also confirmed that the treated soil maintains approximately its pre-blast geotechnical
681 properties, while the natural untreated soil developed lower values that later recovered with time.
682 After blasting, some temporary RAP modifications were also detected by the electrical resistivity
683 profiles and topographical surveys in correspondence with the piers that showed lower stiffness
684 during the construction procedure.

685 Further in-depth data analysis is necessary to understand the fundamental mechanisms leading to
686 the reduction in settlement within the treated panel that may be related to soil densification,
687 increased lateral stress, and composite soil-column behavior during reconsolidation.

688

689 **Acknowledgements**

690 The study was primarily funded by Geopier® Foundation Company (Davidson, North Carolina,
691 United States). A special thanks also to Releo s.r.l. (Ferrara, Italy) who provided the installation of
692 the Rammed Aggregate Piers free of charge. Financial contributions to this research activity were
693 provided by INGV-FIRB Abruzzo project (“Indagini ad alta risoluzione per la stima della
694 pericolosità e del rischio sismico nelle aree colpite dal terremoto del 6 aprile 2009”,
695 <http://progettoabruzzo.rm.ingv.it/it>), by INGV-Abruzzo Region project (“Indagini di
696 geologia, sismologia e geodesia per la mitigazione del rischio sismico”, L.R. n. 37/2016), by CIRI
697 Edilizia e Costruzioni, University of Bologna, Italy (TIRISICO PROJECT “Tecnologie Innovative
698 per la riduzione del rischio sismico delle Costruzioni”, Project no. PG/2015/ 737636, POR-FESR
699 2014-2020), and by FAR UNIMORE 2018 “Sand liquefaction phenomena induced by seismic
700 events: an interdisciplinary approach for assessing the liquefaction potential and improving
701 resilience to earthquake-induced disasters”.

702 Special thanks to Brigham Young University for contributing to the realization of the blast test
703 experiment in terms of personnel and technical equipment; to Scan&Go srl (Massimo Secchia) for
704 the valuable help in TLS surveying by means of the Level Lift Roof -LP16R device for instrument
705 installation; to Image SpA (Giorgio Amendolara) for data analysis and assistance in surveying
706 operations; to the technicians from different Universities and Companies (Dave Anderson, Mario
707 Marcolongo, Alessandro Lodi, Giovanni Bianchi, Gianni Petitti, Luigi Antonetti, Cristiano
708 Prosperi) that helped in the execution and elaboration of the geotechnical and geophysical tests.

709 A special thanks also to Michele Perboni who kindly guested the experimental activities, to the
710 Bondeno Municipality (in particular Stefano Ansaloni, Olga Mantovani and Elena Bonora) and to

711 the Emilia-Romagna Region (Luca Martelli), who provided all the necessary support to realize the
712 research in collaboration with the other local authorities (Ferrara Prefecture, Ferrara Province, Local
713 Civil Protection, Police).

714 The authors would also like to thank the anonymous reviewers for the valuable comments and
715 suggestions to improve the article.

716

717 **References**

718 Adalier, K., Elgamal, A., 2004. Mitigation of liquefaction and associated ground deformations by
719 stone columns. *Engineering Geology* 72: 275-291.

720 Adalier, K., Elgamal, A., Meneses, J., Baez, J.I., 2003. Stone columns as liquefaction
721 countermeasure in non-plastic silty soils. *Soil Dynamics and Earthquake Engineering* 23: 571-584.

722 Alexander, G., Arefi, J., Geoffrey, R.M., 2017. Performance of a stone column foundation system
723 subjected to severe earthquake shaking. *Proceedings of the 3rd International Conference on*
724 *Performance-based Design in Earthquake Geotechnical Engineering - PBD-III*, Vancouver, Canada.

725 Amoroso, S., Milana, G., Rollins, K.M., Comina, C., Minarelli, L., Manuel, M.R., Monaco, P.,
726 Franceschini, M., Anzidei, M., Lusvardi, C., Cantore, L., Carpena, A., Casadei, S., Cinti, F.R.,
727 Civico, R., Cox, B.R., De Martini, P.M., Di Giulio, G., Di Naccio, D., Di Stefano, G., Facciorusso,
728 J., Famiani, D., Fiorelli, F., Fontana, D., Foti, S., Madiati, C., Marangoni, V., Marchetti, D.,
729 Marchetti, S.L., Martelli, L., Mariotti, M., Muscolino, E., Pancaldi, D., Pantosti, D., Passeri, F.,
730 Pesci, A., Romeo, G., Sapia, V., Smedile, A., Stefani, M., Tarabusi, G., Teza, G., Vassallo, M.,
731 Villani, F., 2017. The first Italian blast-induced liquefaction test (Mirabello, Emilia-Romagna,
732 Italy): description of the experiment and preliminary results. *Annals of Geophysics* 60(5), S0556.
733 <https://doi.org/10.4401/ag-7415>.

734 Amoroso, S., Rollins, K.M., Monaco, P., Holtrigter, M., Thorp, A., 2018. Monitoring ground
735 improvement using the seismic dilatometer in Christchurch, New Zealand. *Geotechnical Testing*
736 *Journal* 41(5), 946-966. <https://doi.org/10.1520/GTJ20170376>.

737 Amoroso, S., Rollins, K.M., Andersen, P., Gottardi, G., Tonni, L., García Martínez, M.F.,
738 Wissmann, K., Minarelli, L., 2019. Full-scale testing of liquefaction mitigation using rammed
739 aggregate piers in silty sands. Proceedings of the 7th International Conference on Earthquake
740 Geotechnical Engineering – 7 ICEGE, Rome, Italy, 656-663.

741 Amoroso, S., Comina, C., Marchetti, D., 2020. Combined P- and S-wave measurements by seismic
742 dilatometer test (SPDMT): a case history in Bondeno (Emilia Romagna, Italy). Geotechnical
743 Testing Journal 43(2). <https://doi.org/10.1520/GTJ20180233>.

744 Ashford, S., Rollins, K.M., Lane, J., 2004. Blast-induced liquefaction for full-scale foundation
745 testing. Journal of Geotechnical and Geoenvironmental Engineering 130(8), 798-806.

746 ASTM D2487-11, 2011. Standard practice for classification of soils for engineering purposes
747 (Unified Soil Classification System). West Conshohocken, PA: ASTM International.

748 Caputo, R., Poli, M.E., Minarelli, L., Rapti, D., Sboras, S., Stefani, M., Zanferrari, A., 2016.
749 Palaeoseismological evidence for the 1570 Ferrara earthquake, Italy. Tectonics 35(6), 1423-1445.

750 Civico, R., Brunori C.A., De Martini P.M., Pucci S., Cinti F.R., Pantosti D., 2015. Liquefaction
751 susceptibility assessment in fluvial plains using airborne LIDAR: the case of the 2012 Emilia
752 earthquake sequence area (Italy). Natural Hazards and Earth System Sciences 15, 2473–2483.

753 Cubrinovski, M., Bray, J.D., de la Torre, C., Olsen, M., Bradley, B., Chiaro, G., Stocks, E.,
754 Wotherspoon, L., Krall, T., 2018. Liquefaction-induced damage and CPT characterization of the
755 reclamations at CentrePort, Wellington. Bulletin of the Seismological Society of America, 108(3B),
756 1695–1708. DOI: 10.1785/0120170246.

757 De Martini, P.M., Cinti, F.R., Cucci, L., Smedile, A., Pinzi, S., Brunori, C.A., Molisso, F., 2012.
758 Sand volcanoes induced by the April 6th 2009 Mw 6.3 L’Aquila earthquake: a case study from the
759 Fossa area, Italian Journal of Geosciences 131, 410-422.

760 Emergeo Working Group, 2013. Liquefaction phenomena associated with the Emilia earthquake
761 sequence of May-June 2012 (Northern Italy). Natural Hazards and Earth System Sciences 13(4),
762 935-947.

763 Finno, R.J., Gallant, A.P., Sabatini, P.J., 2016. Evaluating ground improvement after blast
764 densification at the Oakridge landfill. *Journal of Geotechnical and Geoenvironmental Engineering*
765 142(1), 04015054.

766 Fontana, D., Lugli, S., Marchetti Dori, S., Caputo, R., Stefani, M., 2015. Sedimentology and
767 composition of sands injected during the seismic crisis of May 2012 (Emilia, Italy): clues for source
768 layer identification and liquefaction regime. *Sedimentary Geology* 325, 158-167.

769 Fontana, D., Amoroso, S., Minarelli, L., Stefani, M., 2019. Sand liquefaction phenomena induced
770 by a blast test: new insights from composition and texture of sands (late Quaternary, Emilia, Italy).
771 *Journal of Sedimentary Research* 89(1),13-27, <https://doi.org/10.2110/jsr.2019.1>.

772 Gianella, T.N., Stuedlein, A., 2017. Performance of Driven Displacement Pile–Improved Ground in
773 Controlled Blasting Field Tests. *Journal of Geotechnical and Geoenvironmental Engineering*
774 143(9), 04017047.

775 Giona Bucci, M., Villamor, P., Almond, P., Tuttle, M., Stringer, M., Ries, W., Smith, C., Hodge,
776 M., Watson, M., 2018. Associations between sediment architecture and liquefaction susceptibility
777 in fluvial settings: The 2010–2011 Canterbury Earthquake Sequence, New Zealand. *Engineering*
778 *Geology* 237, 181-197.

779 Green, R.A., Olgon, C.J., Wissmann, K.J., 2008. Shear stress redistribution as a mechanism to
780 mitigate the risk of liquefaction. *Proceedings of the 4th Geotechnical Earthquake Engineering and*
781 *Soil Dynamics Conference: Liquefaction Triggering, Consequences, and Mitigation*, Sacramento,
782 California, GSP 181.

783 Harada, K., Orense, R.P., Ishihara, K., Mukai, J., 2010. Lateral stress effects on liquefaction
784 resistance correlations. *Bulletin of the New Zealand Society for Earthquake Engineering* 43(1), 13-
785 23.

786 Hwang, S., Roberts, J.N., Stokoe, K.H. II, Cox, B.R., van Ballegooy, S., Soutar, C., 2017. Utilizing
787 direct-push crosshole seismic testing to verify the effectiveness of shallow ground improvements: a

788 case study involving low-mobility grout columns in Christchurch, New Zealand, Proceedings of
789 Grouting 2017, Honolulu, Hawaii, 415-424.

790 Jamiolkowski, M., Lo Presti D.C.F., Manassero, M., 2003. Evaluation of relative density and shear
791 strength of sands from cone penetration test and flat dilatometer test. Proceedings of Soil Behaviour
792 and Soft Ground Construction, GSP 119, 201-238.

793 Li, H., Liu, S., Tong, L., Xu, X., 2018. Investigating the resonant compaction effect on laterally
794 loaded piles in layered soil. Engineering Geology 246: 1-11.

795 Luzi, L., Pacor, F., Ameri, G., Puglia, R., Burrato, P., Massa, M., Augliera, P., Franceschina, G.,
796 Lovati, S., Castro, R., 2013. Overview on the strong-motion data recorded during the May–June
797 2012 Emilia seismic sequence. Seismological Research Letters 84(4), 629-644.

798 Mahvelati, S., Coe, J.T., Stuedlein, A.W., Asabere, P., Gianella, T.N., 2016. Time-rate variation of
799 the shear wave velocity (site stiffness) following blast- induced liquefaction. Proceedings of
800 Proceedings of GeoChicago, Chicago, Illinois, 904–913.

801 Marchetti, D., Monaco, P., Amoroso, S., Minarelli, L., 2019. In situ tests by Medusa DMT.
802 Proceedings of the XVII European Conference on Soil Mechanics and Geotechnical Engineering
803 ECSMGE-2019, Reykiavik, Iceland, DOI: 10.32075/17ECSMGE-2019-0657.

804 Maurer, B.W., Green, R.A., Wotherspoon, L.M., Bastin, S., 2019. The stratigraphy of compound
805 sand blows at sites of recurrent liquefaction: implications for paleoseismicity studies. Earthquake
806 Spectra, 35(3), 1–20. DOI: 10.1193/041818EQS097M.

807 Minarelli, L., Amoroso, S., Tarabusi, G., Stefani, M., Pulelli, G., 2016. Down-hole geophysical
808 characterization of middle-upper Quaternary sequences in the Apennine Foredeep, Mirabello, Italy,
809 Annals of Geophysics 59(5), S0543. <https://doi.org/10.4401/ag-7114>.

810 Mitchell, J.K., 2008. Mitigation of liquefaction potential in silty sands. Proceedings of From
811 Research to Practice in Geotechnical Engineering Congress 2008, 433-451.

812 Mitchell, J.K., Solymar, Z.V., 1984. Time-dependent strength gain in freshly deposited or densified
813 sand, Journal of Geotechnical Engineering 110(11), 1559-1576.

814 Mitchell, J. K., Wentz, F. L., 1991. Performance of improved ground during the Loma Preita
815 earthquake. Report No. UCB/EERC-91/12, University of California, Berkeley, CA.

816 Narin van Court, W.A., Mitchell, J.K., 1994. Soil improvement by blasting, *Journal of Explosives*
817 *Engineering* 12(3): 34-41.

818 Molinari, I., Argnani, A., Morelli, A., Basini, P., 2015. Development and testing of a 3D seismic
819 velocity model of the Po plain sedimentary basin, Italy. *Bulletin of the Seismological Society of*
820 *America* 105(2A), 753-764.

821 Obermeier, S.F., 1998. Liquefaction evidence for strong earthquakes of Holocene and latest
822 Pleistocene ages in the states of Indiana and Illinois, USA. *Engineering Geology* 50: 227-254.

823 Papathanassiou, G., Mantovani, A., Tarabusi, G., Rapti, D., Caputo, R., 2015. Assessment of
824 liquefaction potential for two liquefaction prone areas considering the May 20, 2012 Emilia (Italy)
825 earthquake. *Engineering Geology* 189, 1-16.

826 Passeri, F., Comina, C., Marangoni, V., Foti, S., Amoroso, S., 2018. Geophysical tests to monitor
827 blast-induced liquefaction, the Mirabello (NE, Italy) test site. *Journal of Environmental and*
828 *Engineering Geophysics* 23(3): 319-333, DOI: 10.2113/JEEG23.3.319.

829 Pesci, A., Amoroso, S., Teza, G., Minarelli, L., 2018. Characterisation of soil deformation due to
830 blast-induced liquefaction by UAV-based photogrammetry and terrestrial laser scanning.
831 *International Journal of Remote Sensing and Remote Sensing Letters* 39(22), 8317–8336.
832 <https://doi.org/10.1080/01431161.2018.1484960>.

833 Pondrelli, S., Salimbeni, S., Perfetti, P., Danecek, P., 2012. Quick regional centroid moment tensor
834 solutions for the Emilia 2012 (northern Italy) seismic sequence. *Annals of Geophysics* 55(4), 615–
835 621. <https://doi.org/10.4401/ag-6146>.

836 Rayamajhi, D., Nguyen, T.V., Ashford, S.A., Boulanger, R.W., Lu, J., Elgamal, A., Shao, L., 2014.
837 Numerical study of shear stress distribution for discrete columns in liquefiable soils. *Journal of*
838 *Geotechnical and Geoenvironmental Engineering* 140(3), 04013034.

839 Rayamajhi, D., Ashford, S.A., Boulanger, R.W., Elgamal, A., 2016. Dense granular columns in
840 liquefiable ground. I: shear reinforcement and cyclic stress ratio reduction. *Journal of Geotechnical*
841 *and Geoenvironmental Engineering* 142(7), 04016023.

842 Robertson, P.K., Wride, C.E., 1998. Evaluating cyclic liquefaction potential using the cone
843 penetration test. *Canadian Geotechnical Journal* 35(3): 442-459.

844 Rollins, K.M., Lane, J.D., Nicholson, P.G., Rollins, R.E., 2004. Liquefaction hazard assessment
845 using controlled blasting techniques, *Proceedings of 11th International Conference on Soil*
846 *Dynamics and Earthquake Engineering*, Berkeley, California, 2: 630 - 637.

847 Saftner, D.A., Green, R.A., Hryciw, R.D., 2015. Use of explosives to investigate liquefaction
848 resistance of aged sand deposits. *Engineering Geology* 199, 140-147.

849 Saftner, D.A., Zheng, J., Green, R.A., Hryciw, R., Wissmann, K., 2018. Rammed aggregate pier
850 installation effect on soil properties. *Institution of Civil Engineers-Ground Improvement* 171(2), 63-
851 73.

852 Salgado, R., Boulanger, R.W., Mitchell, J.K., 1997. Lateral stress effect on CPT liquefaction
853 resistance correlations. *Journal of Geotechnical and Geoenvironmental Engineering* 123(8), 726-
854 735.

855 Smith, M.E., Wissmann, K., 2018. Ground improvement reinforcement mechanisms determined for
856 the Mw 7.8 Muisne, Ecuador, earthquake. *Proceedings of the 5th Geotechnical Earthquake*
857 *Engineering and Soil Dynamics Conference: Liquefaction Triggering, Consequences, and*
858 *Mitigation - GEESDV 2018*, Austin, Texas, GSP 290, 286-294.

859 Stefani, S., Minarelli, L., Fontana, A., Hajdas, I., 2018. Regional deformation of Late Quaternary
860 fluvial sediments in the Apennines foreland basin (Emilia, Italy), *International Journal of Earth*
861 *Sciences*, 107(7), 2433–2447. DOI:10.1007/s00531-018-1606-x.

862 Tonni, L., Gottardi, G., Amoroso, S., Bardotti, R., Bonzi, L., Chiaradonna, A., d’Onofrio, A.,
863 Fioravante, V., Ghinelli, A., Giretti, D., Lanzo, G., Madiati, C., Marchi, M., Martelli, L., Monaco,
864 P., Porcino, D., Razzano, R., Rosselli, S., Severi, P., Silvestri, F., Simeoni, L., Vannucchi, G.,

865 Aversa, S., 2015. Interpreting the deformation phenomena triggered by the 2012 Emilia seismic
866 sequence on the Canale Diversivo di Burana banks, *Rivista Italiana di Geotecnica* 49(2), 28-38.
867 http://www.associazionegeotecnica.it/sites/default/files/rig/2_2015_028ton.pdf

868 Toscani, G., Burrato, P., Di Bucci, D., Seno, S., Valensise, G., 2009. Plio-Quaternary tectonic
869 evolution of the northern Apennines thrust fronts (Bologna-Ferrara section, Italy): seismotectonic
870 implications. *Italian Journal of Geosciences*, 128, 605-613.

871 Vautherin, E., Lambert, C., Barry-Macaulay, D., Smith, M., 2017. Performance of rammed
872 aggregate piers as a soil densification method in sandy and silty soils: experience from the
873 Christchurch rebuild, *Proceedings of the 3rd International Conference on Performance-based*
874 *Design in Earthquake Geotechnical Engineering - PBD-III*, Vancouver, Canada.

875 Wentz, F.J., van Ballegooy, S., Rollins, K.M., Ashford, S.A., Olsen, M.J., 2015. Large scale testing
876 of shallow ground improvements using blast-induced liquefaction, *Proceedings of the 6th*
877 *International Conference on Earthquake Geotechnical Engineering - 6ICEGE*, Christchurch, New
878 Zealand.

879 Wissmann, K.J., van Ballegooy, S., Metcalfe, B.C., Dismuke, J.N., Anderson, C.K., 2015. Rammed
880 aggregate pier ground improvement as liquefaction method in sandy and silty soils. *Proceedings of*
881 *the 6th International Conference on Earthquake Geotechnical Engineering - 6ICEGE*, Christchurch,
882 New Zealand.

883 Wotherspoon, L.M., Cox, B.R., Stokoe, K.H. II, Ashfield, D.J., Phillips, R.A., 2015. Utilizing
884 direct-push crosshole testing to assess the effectiveness of soil stiffening caused by installation of
885 stone columns and rammed aggregate piers, *Proceedings of the 6th International Conference on*
886 *Earthquake Geotechnical Engineering - 6ICEGE*, Christchurch, New Zealand.

887 Zhang, G., Robertson, P.K., Brachman, R.W.I., 2002. Estimating liquefaction-induced ground
888 settlements from CPT for level ground. *Canadian Geotechnical Journal*, 39: 1168-1180. DOI:
889 10.1139/T02-047